NTNU
Norwegian University of
Science and Technology

Tidal boundary layer flow over a flat bottom with vegetation

Marius Holmemo

Marine Technology
Submission date: January 2016
Supervisor: Dag Myrhaug, IMT
Co-supervisor: Lars Erik Holmedal, IMT

Norwegian University of Science and Technology
Department of Marine Technology

NTNU Trondheim
Norwegian University of Science and Technology
Department of Marine Technology – Group of Marine Structures

MASTER THESIS IN MARINE TECHNOLOGY

AUTUMN 2015

FOR

STUD. TECHN. MARIUS HOLMEMO

TIDAL BOUNDARY LAYER FLOW OVER A FLAT BOTTOM WITH VEGETATION

Tidal boundary layer flow in the ocean is of fundamental interest as it is important for transport of e.g. plankton, larvae, contaminated ballast water from ships, oil spills and sea bottom material. These flow components also represent important contributions in physical models for predicting flow circulations in coastal zones and on continental shelves. A proper description of the sea bottom is crucial for good predictions of the flow. In general vegetation is part of the bottom conditions.

The student shall:

1. Give an overview of the mechanisms generating and governing the tidal flows.
2. Give an overview of how to represent vegetation in tidal flow modelling.
3. Investigate the tidal flow by using a one-dimensional two-equation turbulence closure model by first giving a background description of turbulence modelling and the computational tool.
4. Compare data from laboratory measurements including vegetation with numerical predictions.
5. Perform numerical simulations of tidal flow by comparing with field measurements from the Hebrides, including analysis and discussion of the results.

The work scope may prove to be larger than initially anticipated. Subject to approval from the supervisor, topics may be deleted from the list above or reduced in extent.

In the thesis the candidate shall present his personal contribution to the resolution of problem within the scope of the thesis work.

Theories and conclusions should be based on mathematical derivations and/or logic reasoning identifying the various steps in the deduction.

The candidate should utilize the existing possibilities for obtaining relevant literature.

The thesis should be organized in a rational manner to give a clear exposition of results, assessments, and conclusions. The text should be brief and to the point, with a clear language. Telegraphic language should be avoided.

The thesis shall contain the following elements: A text defining the scope, preface, list of contents, summary, main body of thesis, conclusions with recommendations for further work, list of symbols

and acronyms, reference and (optional) appendices. All figures, tables and equations shall be numerated.

The supervisor may require that the candidate, in an early stage of the work, present a written plan for the completion of the work. The plan should include a budget for the use of computer and laboratory resources that will be charged to the department. Overruns shall be reported to the supervisor.

The original contribution of the candidate and material taken from other sources shall be clearly defined. Work from other sources shall be properly referenced using an acknowledged referencing system.

The thesis shall be submitted in two copies:

- Signed by the candidate
- The text defining the scope included
- In bound volume(s)
- Drawings and/or computer prints which cannot be bound should be organized in a separate folder.

Advisors: Research Professor Lars Erik Holmedal
Dr. Hong Wang
Pierre-Yves Henry
Professor Dag Myrhaug

Deadline: 19.01.2016

Dag Myrhaug
Supervisor

Preface

This is my final work in the process of completing my Master of Science degree in Marine Technology here at NTNU.

It has been an interesting and challenging journey. I feel particularly lucky with my choice of topic for this final work, where I have had the opportunity to study both the field of oceanography and the field of computational fluid dynamics. Although oceanography was a new field for me, I feel fortunate to have been introduced to it.

The opportunity to work with, and modify, the numerical FORTRAN code provided by Research Professor Lars Erik Holmedal has given me a thorough understanding of the way the governing equations are discretized and solved. I consider this an advantage as most commercial codes are enclosed and don't allow for the user to interfere, let alone understand, the way they are build.

I want to express my gratitude towards the people who have invested their time and effort into guiding me through this thesis; Professor Dag Myrhaug, Reasearch Professor Lars Erik Holmedal, Dr. Hong Wang and Pierre-Yves T Henry. Their participation and contribution of knowledge has been invaluable. Especially, I want to thank Lars Erik Holmedal for all the help he has provided with the numerical code, and for always taking the time to answer my questions when showing up at his office unannounced. I feel truly grateful to have had the opportunity to learn from and work with this team of highly knowledgeable and driven researchers.

Trondheim, January 19, 2016

Marius Holmemo

Abstract

A one dimensional numerical model with a k-ε closure has been modified to account for the presence of submerged aquatic vegetation when modelling tidal boundary layers. The model has previously been compared against field measurements taken outside the coast of the Hebrides, but did not manage to accurately predict the boundary layer for most part of the water column. Especially the velocity closest to the sea bed was heavily overpredicted.

The goal of this study has been to find a way to reasonably incorporate the effect of vegetation into the already existing numerical model, and to investigate if this modification will improve the accuracy of the predicted tidal boundary layer.

By first studying how the flow mechanisms are being altered due to the presence of a submerged canopy (meadow of individual plants), consensus was found that they best could be accounted for by spatially averaging the governing equations in addition to the common temporal averaging. This way the spatial heterogeneity of the flow due to the complex geometry of the canopy would be accounted for.

The spatial averaging results in an additional form drag term in the momentum equation. In the conservation equation for turbulent kinetic energy, the spatial averaging result in an additional production term. This term accounts for the generation of turbulence in the wakes behind individual stems. Due to this extra production of turbulent kinetic energy, an additional production term of the dissipation of this energy had to be included into the conservation equation for the dissipation.

The modified model was validated against flume experiments, and the results from other available k-ε models, for unidirectional flow through submerged vegetation. The comparison against the other numerical models was good. The comparison against flume experiments showed that the model was able to predict the velocity profiles within the canopy well. However, the accuracy regarding the above-canopy flow appeared to depend on the density of the canopy. However, comparison with flume data for a wider spread of canopy densities has to be preformed before any concluding statements can be made. Overall, the results from the validation was promising.

The model was also modified to account for wave-current damping, and validated against available flume data. The results were good. However, the pressure gradient needed to drive the wave-current flow had to be significantly larger than the pressure gradient needed to drive a pure current with similar depth averaged velocity. Therefore, more research is needed to draw any applicability conclusions for including wave-current interaction into the tidal model.

The modelled vegetation for the tidal flow was very sparse. Because no accurate data for the canopy outside the Hebrides was available during this study, the canopy parameters had to be estimated visually from an underwater photo. Therefore, different canopy parameters was tested to investigate the sensitivity towards the predicted boundary layer.

Overall, the modified model was able to predict the tidal boundary layer with increased

accuracy compared to only accounting for the vegetation in the bed roughness. Especially, the mean velocity closest to the bed was significantly improved as opposed to the old model. However, the results from only including the bed roughness gave increased accuracy for the data point closest to the surface. In comparison, the present model underpredicted the mean velocity in this region.

Although the exact geometry of the vegetation is uncertain, the concluding remark is that the general result is better when directly accounting for the vegetation as opposed to only using the bed roughness. Especially if the main area of interest is the lower part of the tidal boundary layer.

Sammendrag

En endimensjonal k-ε model har blitt modifisert for å ta hensyn til neddykket vegetasjon i beregninger av grensesjikt for tidelvannsstrøm langs en flat havbunn. Modellen har tidligere blitt brukt til å modellere grensesjiktet til tidevannsmålinger fra kysten utenfor Hebridene, men har ikke presterte å generere nøyaktige resultater for mesteparten av vannsøylen. Spesielt hastighetene for området nær havbunnen er ikke godt reprodusert av denne modellen.

Målet med dette arbeidet har vært å finne en fornuftig måte å ta hensyn til effekten av vegetasjon i likningene for k-ε modellen, i tillegg til å studere om disse endringene bidrar til bedre resultater i forhold til feltmålingene.

Fra litteraturen ble det det funnet at den mest hensiktsmessige måten å inkludere effekten av vegetasjon i likningene på er gjennom å integrere dem over flatearealet til et tilstrekkelig stort område. På den måten vil heterogeniteten i strømmen på grunn av geometrien til vegetasjonen bli tatt hesyn til i likningene. Dette blir gjort i tillegg til den vanlige tidsintegreringen for å fjærne de tidsavhengige flukture ringene til den turbulente strømmen.

Denne metoden fører til et nytt ledd i konserveringslikningene for moment på grunn av formmotstand mellom strømmen og plantene. I tillegg fører det til et nytt produksjonsledd av turbulent kinetisk energi på grunn av turbulens som dannes i waken bak individuelle planter. På grunn av den økte produksjonen av turbulens vil også konserveringslikningen for dissipasjonen av denne energien få ett nytt produksjonsledd.

Gjennom validasjon mot eksperimentelle data, samt resultater fra andre k-ε modeller, ble det funnet at den modifiserte modellen ga god overenstemmelse med de tilgjengelige sammenlikningsdataene. Hastighetene inne i vegetasjonen ble godt modellert av modellen, mens hastighetene over vegetasjonen ga indikasjoner på at de kan være avhengig av selve tettheten til plantefeltet. Flere sammenlikninger trengs for å bekrefte denne påstanden. Totalt sett var validajonen vellykket.

Effekten av bølge-strøm dempning ble også lagt til koden for sammenlikning med eksperimentelle data. Det ble funnet at den nødvendige trykkgradienten for å drive strøm med bølger måtte være betydelig større enn den nødvendige trykkgradienten for å drive en ren strøm med tilsvarende dybdemidlet hastighet. Det er derfor behov for mer validering av bølge-strøm interaksjonen før den kan bli tilført tidevannsmodellen.

Vegetasjonen utenfor kysten av Hebridene er veldig spredt. De nødvendige vegetasjonsparameterene måtte estimeres ettersom ingen nøyaktig data var tilgjengelig i løpet dette arbeidet. Den modifiserte modellen har derfor blitt kjørt med ulike inputdata for vegetasjonen for å danne en formening om i hvilken grad resultatene blir påvirket av disse parameterene.

Den modifiserte modellen viser at den generelt presterer å generere et grensesjiksprofil i større samsvar med måledataen enn den gamle modellen som bare tar hensyn til ruheten på bunnen. Spesielt vil strømhastighetene nært bunnen blir bedre predikert av den modi-

fiserte modellen. For målepunktet nærmest overflaten vil den gamle modellen gi en bedre estimering av strømhastighetene.

Selv om det er en usikkerhet knyttet til inputparameterene for vegetasjonen, vil den generelle konklusjonen være at grensesjiktsprofilet blir bedre estimert av å direkte inkludere effekten av vegetasjonen i modellen, sammenlignet med bare å ta hensyn til den i estimatet av ruheten på bunnen. Dette viser seg å gjelde til og med for veldig spredt vegetasjon som tilfellet er utenfor Hebridene. Spesielt hvis hastighene nært bunnen er av størst interesse, vil en inkluderingen av vegetasjonene være betydelig for nøyaktigheten av tidevannsprofilet.

Contents

Figures

Tables

Abbreviations

CFD	Computational Fluid Dynamics
RANS	Reynolds Average Navier-Stokes
LES	Large Eddy Simulation
DNS	Direct Numerical Simulation
DES	Detached Eddy Simulation
DDES	Delayed Detached Eddy Simulation
IDDES	Improved Delayed Detached Eddy Simulation
AWAC	Acoustic Wave And Current
EMF	Electromagnetic Flow Meter
ADV	Acoustic Doppler Velocimetry

Symbols

Note that some symbols may be given more than one meaning throughout the text.

$\mathbf{r}_P$	Position vector of a point P on Earth relative to the Sun
$\mathbf{r}_E$	Position vector of the rotational centre of Earth relative to the Sun
$\mathbf{r}_{P/E}$	Position vector of a point P relative to the rotational centre of Earth
$\mathbf{a}_P$	Absolute acceleration of a point P
$\mathbf{a}_E$	Acceleration of Earth relative to the Sun
$\dot{\boldsymbol{\omega}}$	Angular acceleration of Earth
$\mathbf{r}$	Position vector of a point P relative to the rotational centre of Earth
$\boldsymbol{\omega}$	Angular velocity of Earth
$\mathbf{v}_{rel}$	Translational velocity of a point P relative to Earth
$\mathbf{a}_{rel}$	Translational acceleration of a point P relative to Earth
m	Earth's mass
$\mathbf{F}$	Force vector
a_c	Magnitude of the Coriolis acceleration
v_{rel}	Magnitude of the relative velocity between a point P and Earth
θ	Latitude
f	Coriolis parameter
L	Characteristic length
u_0	Characteristic velocity
f_0	Coriolis parameter at a given latitude
R_0	The Rossby number
$\boldsymbol{\Omega}$	Angular acceleration of the Earth-Moon system
$\mathbf{a}_T$	Translational acceleration of the Earth-Moon system relative to the Sun
$\mathbf{a}_E$	Position vector of Earth's centre of rotation relative to Earth-Moon system
$\mathbf{S_0}$	Centrifugal force
$\mathbf{G}$	Gravitational force
G	Gravitational constant
M	Mass of Moon
$\mathbf{R}$	Position vector between a point P and the Moon
$\mathbf{T}$	Tidal force
$\mathbf{G}_0$	Gravitational force acting on Earth from the Moon
M_2	Principal lunar semidiurnal tidal constituent
N_2	Larger lunar elliptic semidiurnal tidal constituent
L_2	Smaller lunar elliptic semidiurnal tidal constituent
S_2	Principal solar semidiurnal tidal constituent
x,y,z	Coordinate axis
u,v,w	Velocity components in x-, y- and z-direction
ρ	Water density
ν	Kinematic viscosity
$\overline{u}_i$	Temporal mean velocity
u_i'	Temporal fluctuating velocity
p	Pressure

$\overline{p}$	Temporal mean pressure
p'	Temporal fluctuating pressure
$\overline{u_i' u_j'}$, τ_{ij}	Reynolds stress
k	Turbulent kinetic energy
δ_{ij}	Kronecker delta
ν_t	Eddy/turbulent viscosity
$\overline{p}_n$	Temporal mean pressure
l_e	Characteristic eddy length scale
V_e	Characteristic eddy velocity scale
ε	Dissipation of turbulent kinetic energy
C_μ	Eddy viscosity constant
$C_{\varepsilon 1}$	k-ε constant
$C_{\varepsilon 2}$	k-ε constant
σ_k	k-ε constant
σ_ε	k-ε constant
u_*	Friction velocity
κ	Constant
E	Roughness parameter
z^+	Nondimensional length
u^+	Nondimensional velocity
z_0	Bottom roughness
k_n	Nikuradse roughness
z_a	Bottom roughness due to wave-current interaction
τ_w	Laminar shear stress
H	Water depth
h	Canopy height
ΔS	Average distance between plant stems
d	Stem diameter
a	Frontal area per volume of a representative plant
λ_f	Roughness density
ϕ	Solid volume fraction
C_D	Canopy drag coefficient
δ_e	Canopy-scale vortices penetration depth
$\langle u_i \rangle$	Spatial mean velocity
u_i''	Spatially fluctuating velocity
$\langle p \rangle$	Spatial mean pressure
p''	Spatially fluctuating pressure
$\langle \overline{u}_i \rangle$	Spatial mean of the time averaged velocity
$\overline{u}_i''$	Spatial fluctuation of the time averaged velocity
$\langle \overline{p} \rangle$	Spatial mean of the time averaged pressure
$\overline{p}''$	Spatial fluctuation of the time averaged pressure
$\langle \overline{u}_i'' \overline{u}_j'' \rangle$	Dispersive stress/flux
f_V	Viscous drag
$\bigtriangledown$	Laplace operator
f_D	Form drag
P_w	Turbulent wake-production

Re	Reynolds number
U	Stem inflow velocity
C_{fk}	Wake-production coefficient
D_w	Wake-dissipation
$C_{f\varepsilon}$	Wake-dissipation coefficient
τ_{int}	Effective time scale
τ_{int}	Intrinsic time scale
τ_{geom}	Geometric time scale
L_p	Length scale
A_p	Solid volume fraction
n	Number of stems per bed area
C_1	Shape coefficient
fv	u-component of the Coriolis force
fu	v-component of the Coriolis force
f_{Dx}	x-component of the canopy form drag
f_{Dy}	y-component of the canopy form drag
u_0	Field measurement of u-component of velocity
v_0	Field measurement of v-component of velocity
S	Surface slope
g	Gravitational acceleration
U_{max}	Maximum horizontal velocity for wave-current flow
U_w	Horizontal component of wave particle velocity
U_{mean}	Depth averaged wave-current velocity
U_c	Depth averaged current-velocity
ζ_A	Wave amplitude
T	Wave period
ω	Wave frequency
$\overline{U}$	Depth averaged velocity
ax	Semi-minor axis
by	Semi-major axis
d_s	Stem diameter
d	Plant diameter

1 Introduction

Interaction between gravity forces acting on Earth from the Moon and the Sun, and the relative motion between these masses, produces water surface elevations known as tides. Due to their oscillatory behaviour, tides can be viewed as waves with large wavelengths and long periods called tidal periods. Because of the large wavelength, these tidal waves often act like shallow water waves even at large water depths. The horizontal component of the orbital particle trajectories will in most cases be so dominant that the tidal waves can be regarded as tidal currents instead.

Due to the friction between the tidal current and the sea bed, a boundary layer is formed with a corresponding shear force acting on the bed. This shear force is of importance as it may cause erosion at the sea bed. When this occur, the general shape of the boundary layer becomes important as it determines the capacity the tidal current has to further transport the sediments. In addition to transport of sediments and pollution, the tidal current will also affect the transport of biological material such as plankton, hence impacting the marine life in general.

From the above mentioned reasons, the importance of understanding tidal boundary layers becomes apparent. Much research has gone into the modelling of these boundary layers, along with closely related mechanism such as sediment transport. Numerical models are effective tools for doing so. Because tidal currents often are turbulent, this must also be incorporated into the models.

In near shore regions there is another effect that becomes important in the modelling of tidal boundary layers. Near shore regions are often covered with submerged aquatic vegetation. In terms of erosion and sediment transport this will alter the mechanisms for unobstructed flow by introducing additional damping of the tidal current within the vegetation.

Extensive work has been done in studying oscillatory tidal flow using numerical solvers, but without the presence of vegetation. Apart from one-equation and simpler models, Holmedal and Myrhaug (2013) used the two equation k-ε model to predict the tidal ellipses and velocity time series against field data from the Celtic Sea. The boundary conditions at the surface was then altered to include the shear effects from wind, and sediment transportation with or without wind was investigated. In addition, more computationally expensive methods has been used for modelling oscillatory boundary layers such as LES (Salon and Armenio (2011)) and the DNS (Sakamoto and Akitomo (2008)) methods.

The effect of vegetation upon boundary layers is also a widespread research topic. Foremost this was a topic under meteorology in the study of wind flowing over terrestrial canopies. However, the topic has long since become relevant for the marine and aquatic communities. Most of these studies only consider the effect of the vegetation in open channels or marshlands, and not as part of a tidal system. The word *canopy* is heavily used throughout this thesis, and translates to a meadow of individual plants. This means that the characteristics of a plant may not directly correspond to the characteristics of the whole canopy.

The presence of plants has often been simplified by regarding it as a an addition to the general bed roughness. However, for sufficiently dense aquatic vegetation, it is well established that this is not the case (Nepf (2012a)). For numerical modelling of flow through vegetation, the effect of the vegetation therefore has to be included in a different way. Wilson and Shaw (1977) assumed that the heterogeneity in the flow due to individual plants could be accounted for by spatially averaging the governing equations in addition to the already introduced temporal averaging. Raupach and Shaw (1982) later modified the derivation, although arrived at the same conclusion. The spatial averaging of the momentum equations results in an additional form drag due to the energy extracted from the mean flow due to the work against the plants. Spatial averaging of the conservation equation for turbulent kinetic energy results in an additional production term transforming the energy from the mean flow into additional turbulence in the wakes behind individual plant stems.

Shimizu and Tsujimoto (1994) preformed numerical analysis with a k-ε closure of uniform flow through a submerged canopy. They used the additional terms introduced by the spatial averaging in the momentum and k-equation. An additional term was added to the ε-equation to account for the dissipation of the wake-produced turbulence. The inclusion of the additional terms to the k- and ε-equation introduces additional coefficients to help improve the generality of the model under different vegetation conditions. Shimizu and Tsujimoto (1994) obtained these additional constants by fitting their model results to experimental data from flume experiments. After determining the coefficients, their model was run against additional experimental trails to verify its generality. I addition, the transition zone that appears when flow enters a submerged canopy from a non-vegetated region was investigated.

López and García (2001) used both a k-ε and a k-ω closure to model open channel flow through submerged vegetation. The inclusion of the additional form drag, wake-production and dissipation are similar to Shimizu and Tsujimoto (1994). However, they used a more theoretical approach to determine the additional constants. They found that the k-ε and a k-ω models predicted the flume data with similar accuracy. The same k-ε model was also used to model sediment transport (López and García (1998)).

Defina and Bixio (2005) compared the numerical models from Shimizu and Tsujimoto (1994) and López and García (2001) with an explicit two-layer model. The two-layer model separates the flow into one lower layer governed by the effect of the vegetation and one upper layer treating the vegetation as a roughness. Applying a continuity requirement between the two regions then gives the total velocity profile.

Neary (2003) preformed k-ω simulations for the case of steady state flow through submerged vegetation. Although the model is different from the k-ε model through the numerical solving of the near wall region, the inclusion of the canopy form drag and wake-production is similar. He compared the two different pairs of constants provided by Shimizu and Tsujimoto (1994) and López and García (2001) and found that the they gave similar results for the mean velocity profiles and the Reynolds stress. However, neither pair gave good results for the streamwise turbulence intensity, but the coefficients of Shimizu and Tsujimoto (1994) were considered better. However, this conclusion is somewhat bias due to the fact that their model results were only compared with the flume data

provided by Shimizu and Tsujimoto (1994). The same data they used for determining the coefficients in the first place. Neary (2003) also support the conclusion from López and García (2001) in the sense that the k-ω model gave no significantly better results than the k-ε model.

One of the disadvantages of the numerical models introduced by Shimizu and Tsujimoto (1994), López and García (2001) and Neary (2003) is that they don't account for the additional vortex generation that might occur due to the shear force between the top of the canopy and the unobstructed flow. Uittenbogaard (2003) proposed a modification to the k-ε model to account for this problem. The modification results in an increased production of dissipation within the canopy. Dijkstra and Uittenbogaard (2010) used this modification along with their own force balance to account for the flexibility of vegetation in the k-ε model.

King et al. (2012) proposed a more complex method of incorporating the effect of vegetation into a numerical model. The basic conservation equations was that of the standard k-ε model. However, the conservation of turbulent kinetic energy was split into one conservation equation for the wake-generated turbulence and one conservation equation for the shear generated turbulence. Hence, these two conservation equations had to be solved simultaneously as the shear generated turbulence was transformed into wake-scaled turbulence when interacting with the stem wakes. Correspondingly, two conservation equations for the dissipation had to be solved simultaneously as well. Although the model produced good results, additional coefficients had to be introduced.

Ghisalberti and Nepf (2004) stressed the importance of the shear-generated vortices at the top of the canopy and developed their own numerical model. They neglected the production of wake-scaled turbulence. Instead they developed a conservation equation for the turbulent kinetic energy consisting only of the generation of shear-scale turbulence from the top of the canopy and its dissipation into wake-scale turbulence as the vortices penetrated into the canopy. However, this model is only applicable for steady state flow, and is only valid within the range of the shear-scale, or canopy-scale, vortices.

The model of López and García (2001), along with their proposed coefficients, was developed further by Ma et al. (2013) to incorporate wave propagation through the canopy, and the effect of wave breaking.

In addition to the above-mentioned RANS models, Stoesser (2009) performed LES simulations for submerged rigid cylinders and encountered shear-generated vortices from the top of the canopy affecting the in-canopy flow. This is in agreement with what had been recorded by Ghisalberti and Nepf (2004).

In this study, the numerical k-ε model used by Holmedal and Myrhaug (2013) to predict tidal boundary layers will be modified to account for submerged vegetation. Grønningsæter (2015) compared the model against field measurement from the coast outside the Hebrides, but did not succeed in predicting the lower portion of the tidal boundary layer when only accounting for the bed roughness. Hence, the modified code will be validated and applied to the same field measurements to investigate if the results improve if the effect of vegetation is incorporated into the model.

2 The Coriolis force

The Coriolis force is essential when working with tidal flows. From a numerical modelling perspective it is the only parameter separating a tidal flow from a regular unidirectional flow. In this chapter the Coriolis force will be derived and explained for a point P moving along the Earth's surface.

Earth rotates about its own axis as well as moving relative to the Sun. If P is an object moving along Earth's surface then the absolute position of P can be expressed as

$$\mathbf{r}_P = \mathbf{r}_E + \mathbf{r}_{P/E}. \tag{2.0.1}$$

$\mathbf{r}_E$ is the position of Earth relative to the Sun, and $\mathbf{r}_{P/E}$ is the relative position between P and Earth's centre (see figure 2.1a). By differentiating twice with respect to time, it can be shown (see Meriam and Kraige (2013)) that the absolute acceleration of point P becomes,

$$\mathbf{a}_P = \mathbf{a}_E + \dot{\boldsymbol{\omega}}\times\mathbf{r} + \boldsymbol{\omega}\times(\boldsymbol{\omega}\times\mathbf{r}) + 2\boldsymbol{\omega}\times\mathbf{v}_{rel} + \mathbf{a}_{rel} \tag{2.0.2}$$

where the first three terms are the acceleration of P if P were a fixed point on Earth's surface, and the last two terms are the acceleration of P relative to the Earth's axis. Hence, $\mathbf{a}_E$ is the translational acceleration of the Earth relative to the Sun, and $\mathbf{v}_{rel}$ and $\mathbf{a}_{rel}$ are the translational velocity and acceleration, respectively, of P relative to the Earth's axis. $\mathbf{r}$ is the same as $\mathbf{r}_{P/E}$, and $\boldsymbol{\omega}$ and $\dot{\boldsymbol{\omega}}$ are the angular velocity and acceleration of Earth, respectively.

Because the angular acceleration of Earth around its axis, and the translational acceleration of Earth relative to the Sun are small compared to the other terms, they can be neglected. Hence, $\boldsymbol{\omega} \approx 0$ and $\mathbf{a}_E \approx 0$. Also, the term $\boldsymbol{\omega}\times(\boldsymbol{\omega}\times\mathbf{r})$, acting normal to the Earth's axis, will be approximately zero and hence neglected (see Myrhaug (2012)). The absolute acceleration of an object P moving along the face of the Earth will therefore be simplified to

$$\mathbf{a}_P = \mathbf{a}_{rel} + 2\boldsymbol{\omega}\times\mathbf{v}_{rel}, \tag{2.0.3}$$

where the last term is called the Coriolis acceleration. Because P is moving with the relative velocity $\mathbf{v}_{rel}$, the Coriolis force will always act normal to the path of motion. The total force on P can be written in terms of Newtons 2. law, $\mathbf{F} = m\mathbf{a}_P$, where $\mathbf{F}$ has the same direction as $\mathbf{v}_{rel}$. Utilizing equation (2.0.3) and rearranging gives,

$$m\mathbf{a}_{rel} = \mathbf{F} - m2\boldsymbol{\omega}\times\mathbf{v}_{rel} \tag{2.0.4}$$

Because Earth's rotation is counter clockwise this will result in a Coriolis force acting 90 degrees to the right of the objects path of motion on the Northern hemisphere, and

90 degrees to the left on the Southern hemisphere (see figure 2.1b). At the equator the Coriolis force will be zero. The Coriolis force is not a physical force felt on Earth, but a result of P moving along a rotating reference system.

The magnitude of the Coriolis acceleration is

$$a_c = |2\boldsymbol{\omega}\times\mathbf{v}_{rel}| = 2\omega v_{rel}\sin\theta = f v_{rel}, \tag{2.0.5}$$

where f is the Coriolis parameter and θ is the latitude. Therefore, f is dependent on the latitude the object is moving at.

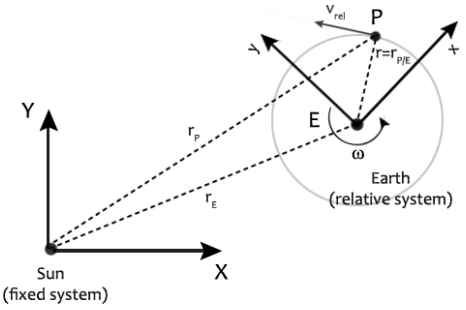

(a) Illustration of the fixed system (the Sun) and the relative system the Earth with an object P moving along the face of the Earth.

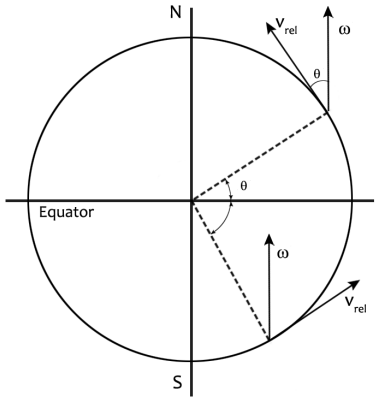

(b) The different vector configurations on the Northern and Southern hemisphere resulting in different directions of the Coriolis force.

Figure 2.1: Reactions from Earth being a relative reference system.

2.1 The Rossby number

When to account for the Coriolis acceleration depends on the relative magnitude between the Coriolis acceleration and $\mathbf{a}_{rel}$. The relative importance between these two acceleration components are expressed by the Rossby number. Looking at a particle travelling in the x-direction with speed u, the inertial acceleration can be expressed as $u(\partial u/\partial x)$. Using a characteristic length L and a characteristic speed u_0 gives $u_0(u_0/L)$. The same analogy for the Coriolis acceleration yields $f_0 u_0$ where f_0 is the Coriolis parameter at the given latitude. Hence the Rossby number becomes

$$R_0 = \frac{u_0}{L f_0}. \tag{2.1.1}$$

When $R_0 >> 1$ the inertial forces are dominating, and vice versa. For the tidal flow modelled in this study it is assumed that $Re << 1$. Hence, the convective terms in the momentum equations can be neglected. This is called the low Rossby number approximation.

3 Tides

Tides are oscillatory water surface elevations. They are created as a result of two extraterrestrial effects, namely the centrifugal force acting on Earth due to the rotation of the Earth-Moon system around its own axis, and the gravitational forces acting on Earth from astronomical objects. The most dominant astronomical object is the Moon, and the second most important is the Sun. The rest of them can normally be neglected.

This chapter will give a simplified mathematical description of why tides occur, and then more effects will be added to explain some of their complexity. The theory in this chapter is adopted from Myrhaug (2012).

The force balance resulting in the generation of tides can be obtained by once again considering the absolute acceleration in equation (2.0.2) of a point P located at the Earth's surface,

$$\mathbf{a}_P = \mathbf{a}_E + \dot{\boldsymbol{\omega}}\times\mathbf{r} + \boldsymbol{\omega}\times(\boldsymbol{\omega}\times\mathbf{r}) + 2\boldsymbol{\omega}\times\mathbf{v}_{rel} + \mathbf{a}_{rel} \tag{3.0.1}$$

Contrary to chapter 2, point P will now refer to a specific location on earth, hence P is not moving relative to Earth. This means that the Coriolis acceleration $\mathbf{a}_c = 2\boldsymbol{\omega}\times\mathbf{v}_{rel}$ and the translational acceleration ($\mathbf{a}_{rel}$) between point P and the Earth's centre disappears. The term $\dot{\boldsymbol{\omega}}\times\mathbf{r}$ is small and can be neglected in accordance with chapter 2. $\boldsymbol{\omega}\times(\boldsymbol{\omega}\times\mathbf{r})$ is directed normal to Earth's rotational axis and does not contribute to any resulting tidal force. Hence, equation (3.0.1) reduces to

$$\mathbf{a}_P = \mathbf{a}_E, \tag{3.0.2}$$

where $\mathbf{a}_P$ is the absolute acceleration of a fixed point P on Earth, and $\mathbf{a}_E$ is the translational acceleration of Earth relative to the Sun. $\mathbf{a}_E$ can be expressed with regards to the acceleration of the Earth-Moon system relative to the Sun. The rotational axis of the Earth-Moon system is at its combined centre of mass, and has the angular acceleration $\boldsymbol{\Omega}$. The system is depicted in figure 3.1.

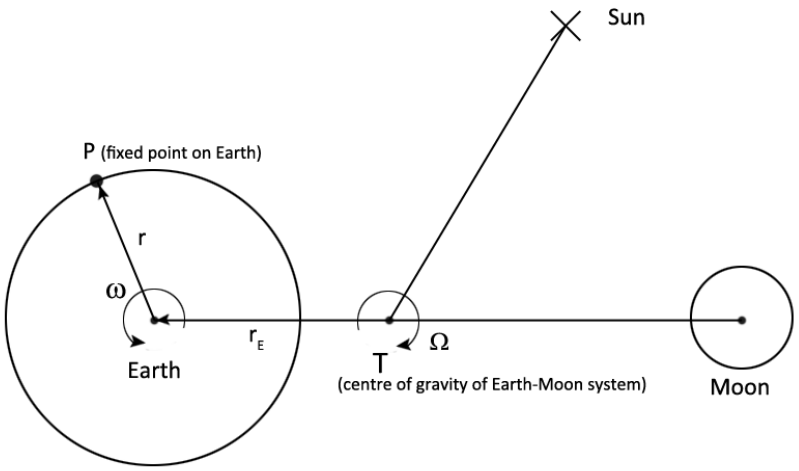

Figure 3.1: Illustration of the rotation of the Earth-Moon system where $\mathbf{\Omega}$ is the angular velocity of the Earth-Moon system around its combined centre of mass, and ω is the angular velocity of the Earth around its own axis. (Reproducted after Myrhaug (2012))

Hence, the absolute acceleration of point P can be expressed as

$$\mathbf{a}_P = \mathbf{a}_E = \mathbf{a}_T + \mathbf{\Omega}\times(\mathbf{\Omega}\times\mathbf{r}_E) \tag{3.0.3}$$

where $\mathbf{a}_T$ is the translational acceleration of the Earth-Moon system relative to the Sun, $\mathbf{\Omega}$ is the angular velocity of the Earth-Moon system, and $\mathbf{r}_E$ is the position of the rotational axis of Earth relative to the rotational axis of the Earth-Moon system.

The translational acceleration $\mathbf{a}_T$ of the Earth-Moon system relative to the Sun can be neglected, leaving the absolute acceleration of a fixed point P on Earth to be

$$\mathbf{a}_P = \mathbf{\Omega}\times(\mathbf{\Omega}\times\mathbf{r}_E). \tag{3.0.4}$$

The acceleration in equation (3.0.4) is the centripetal acceleration working between the rotational axis of the Earth-Moon system and the rotational axis of Earth. On Earth this will be felt as a centrifugal force,

$$\mathbf{S_0} = m\mathbf{\Omega}\times(\mathbf{\Omega}\times\mathbf{r}_E) \tag{3.0.5}$$

where m is the mass of the Earth. As noted, the direction and magnitude of $\mathbf{S_0}$ is independent of the position of P.

The other forces acting on Earth is the gravitational force from the Moon and the Sun. By first considering the effect from the Moon alone, the gravitational force $\mathbf{G}$ on Earth is given by Newton's law of universal gravitation

$$\mathbf{G} = G\frac{mM}{|\mathbf{R}|^2}\frac{\mathbf{R}}{|\mathbf{R}|}, \tag{3.0.6}$$

where G is the gravitational constant, m is the mass of any object or unit at point P, M is the mass of the Moon, and $\mathbf{R}$ is the vector from the centre of the Moon to point P. Contrary to the centrifugal force, the gravitational force varies both in magnitude and direction depending on the position of point P. This creates the resulting tidal force $\mathbf{T}$ along the face of the Earth which forces the water levels to rise. Figure 3.2 shows the resulting force component $\mathbf{T}$ at different locations (P) on Earth denoted with index 0,1 and 2. Only at the centre of the Earth will the centrifugal force be balanced by the gravitational force, $\mathbf{S}_0 = \mathbf{G}_0$.

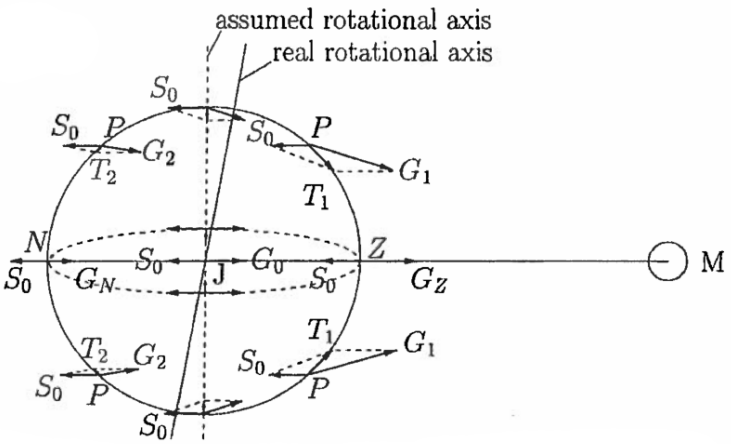

Figure 3.2: Illustration of the resulting tidal force T as it arises at different positions (P) along the face of the Earth. (Myrhaug (2012))

Assuming that the surface of the Earth consist only of water, the tidal force $\mathbf{T}$ will result in a simplified tidal pattern as shown in figure 3.3. As illustrated in both figure 3.2 and 3.3 the rotational axis of Earth is assumed to be perpendicular to the position vector between the centre of Earth and the Moon.

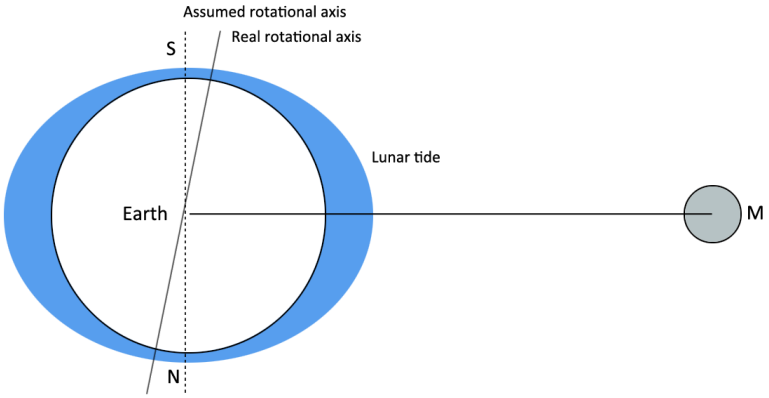

Figure 3.3: Illustration of how the tidal force creates changes in the water surface elevation around Earth.

In addition to the gravitational force from the Moon, the gravitational force due to the Sun must also be accounted for. Figure 3.4 gives a simplified illustrating of how the combined gravitational effect from the Moon and the Sun results in something called a *spring tide* and a *neap tide*. The spring tide occurs when the Earth, the Moon and the Sun are in alignment, while the neap tide occurs when they are in a 90° misalignment.

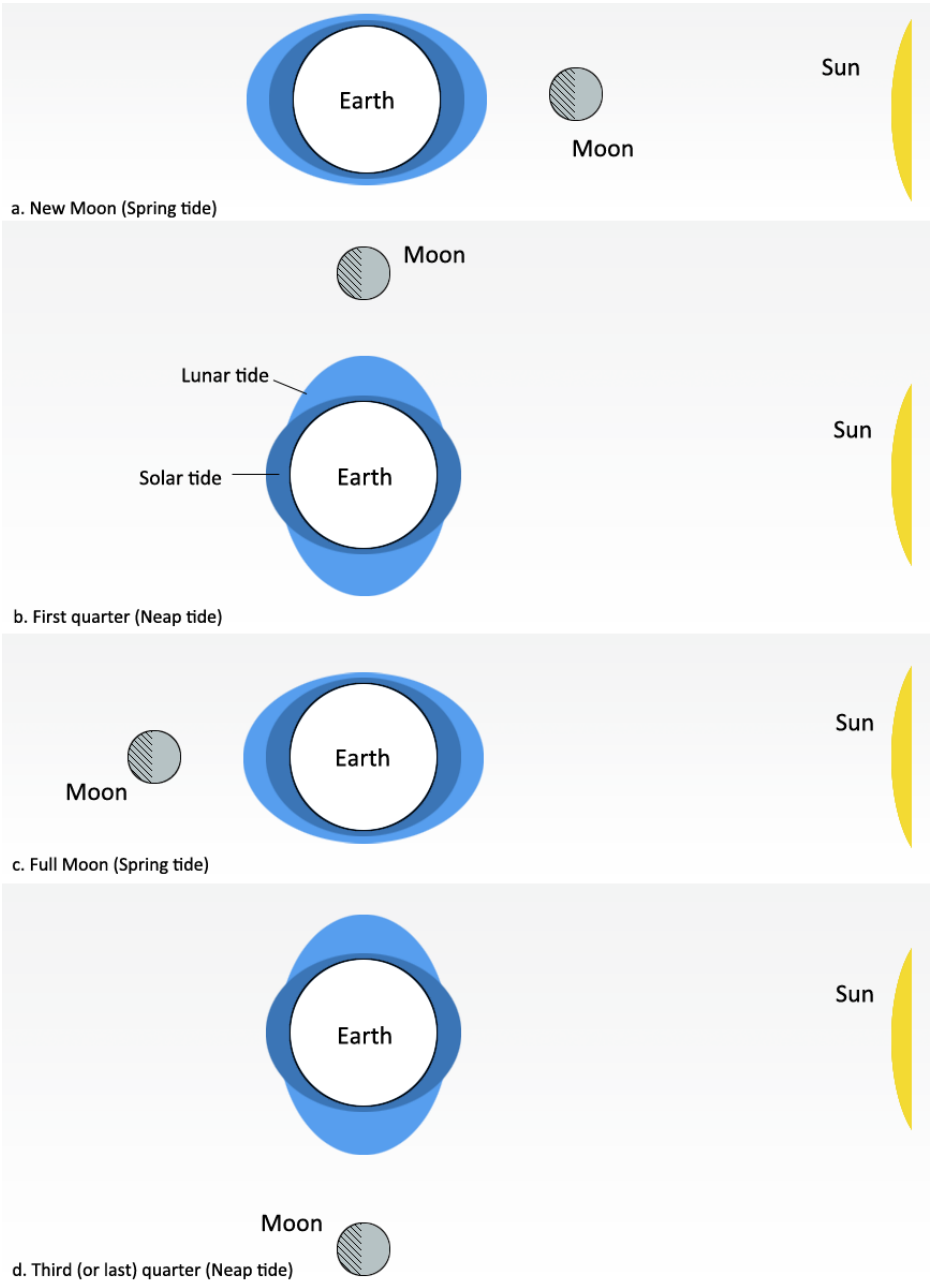

Figure 3.4: Simplified illustration showing the combined effect of the solar and lunar tides (as observed if looking directly down at the North Pole). Their interaction results in a case of high tides (spring tide) when the Earth, the Moon and the Sun are aligned, and a case of low tides (neap tide) when they are in a 90° misalignment. (Reproduced after Myrhaug (2012))

The models described so far are only suitable to describe the generation of the water surface elevations. The tidal system becomes more complex when considering the impact from land areas, ocean topology and that the Earth and the Moon rotates in different planes, as well as following elliptic paths.

Because all the tidal effects are oscillatory, the total tidal effect can be decomposed into different tidal components (or constituents). The tidal components are given letters with index numbering to easily distinguish between the different tidal effects.

M_2 is the tidal component due to the gravitational force from the moon alone. It has a period of 12.42 hours, accounting for the 24 hours rotation of the Earth as well as the small distance travelled by the Moon due to its rotation around Earth. N_2 and L_2 are also tidal components due to the moon, and accounts for the elliptical path of the Earth-Moon system. Similarly, S_2 is the main tidal constituent due to the Sun alone, and has a period of 12 hours due to Earth rotating once around its own axis in 24 hours. There are also tidal constituents to account for the relative declination between the Earth and the Moon, as well as between the Earth and Sun.

The constituents marked with index one are diurnal constituents, meaning that they only peak once every solar-day (24 hours). The constituents marked with index two are semi-diurnal, meaning they peak twice every solar-day. Whether a particular location on Earth has a diurnal or a semi-diurnal tidal system (one or two high tides each day) depends on the resulting tidal system after superposition of all the individual constituents.

Because the tides are oscillating, the Coriolis force will also affect the tidal pattern by deflecting the tidal wave to the right on the northern hemisphere, and to the left on the southern hemisphere. This, along with the constraints by land areas, result in what is known as an *amphidromic systems*. These are tidal waves rotating around an amphidromic point with zero tidal range (zero water elevation). The tidal range increases with distance away from this point. The time it takes for one tidal wave to complete one rotation around the amphidromic point is called the tidal cycle of that particular amphidromic system. A typical amphidromic system is depicted for the North Sea in figure 3.5. The plain lines indicates the rotation of the tidal waves measured in 1/24 of a lunar day (24.84 hours), while the dotted lines indicates the tidal range.

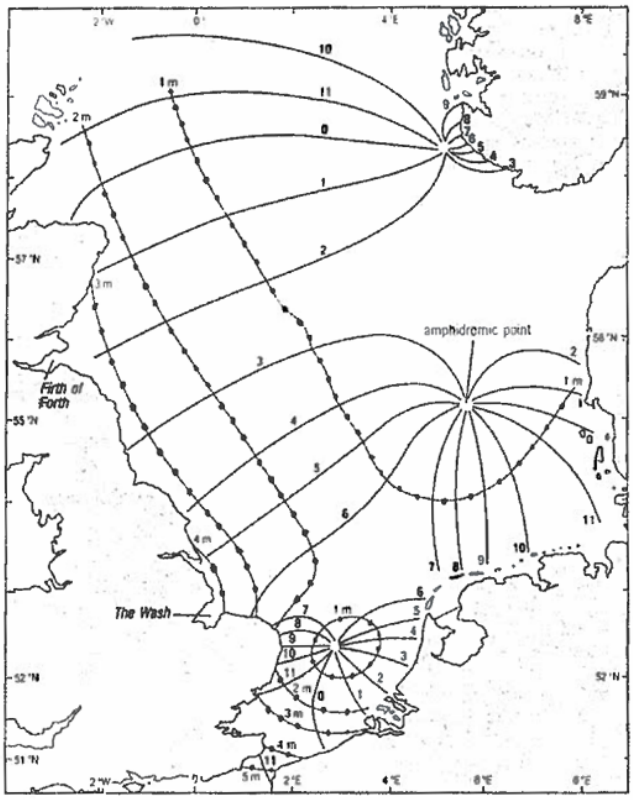

Figure 3.5: Amphidromic system for the North Sea. (Myrhaug (2012))

Although the tidal flows are complex, they are completely predictable.

3.1 Tidal currents

As already indicated, the oscillating tides can be considered as tidal waves, often rotating as part of an amphidromic system. The wave length of these tidal waves are so large that they can be considered as shallow water waves even at large water depths. As opposed to deep water waves where the particle trajectories are circular and decays infinitely towards the sea bed, the shallow wave particle trajectories does not. Instead, they stay elliptical all the way to the sea bed. For tidal waves the vertical velocity component of the elliptical particle trajectories becomes so small that the wave induced flow can be considered as horizontal. Therefore, the wave induced velocities due to a tidal wave can be described as a *tidal current*. The oscillation period of this current is the same as the governing tidal period at the specific location.

4 Turbulence Modelling

4.1 RANS equations

The two governing equation being solved by any CFD solver, when excluding heat transfer, is the continuity equation and the Navier-Stokes equations. For incompressible flow these are expressed in tensor form as (4.1.1) and (4.1.2), respectively.

$$\frac{\partial u_j}{\partial x_j} = 0 \tag{4.1.1}$$

$$\frac{\partial u_i}{\partial t} + u_j \frac{\partial u_i}{\partial x_j} = -\frac{1}{\rho}\frac{\partial p}{\partial x_i} + \frac{\partial}{\partial x_j}\left(\nu\left[\frac{\partial u_i}{\partial x_j} + \frac{\partial u_j}{\partial x_i}\right]\right), \tag{4.1.2}$$

where $x_i = [x, y, z]$ denotes the x- ,y- and z-direction of the flow and $u_i = [u, v, w]$ is the velocity components in each direction, respectively. The Navier-Stokes equations in (4.1.2) are basically Newtons 2. law. The terms on the left hand side are the instantaneous change of velocity and the convection term, while the terms on the right hand side are the pressure gradient and a viscous friction or stress term due to the fluids kinematic viscosity, ν.

For turbulent flow each velocity component can be said to consist of one mean component and one fluctuating component, in time. Therefore the total velocity can be written,

$$u_i = \overline{u}_i + u_i'. \tag{4.1.3}$$

where the overbar represents the mean component and the prime indicates the fluctuating component. The same anology can be used for the pressure, hence

$$p = \overline{p} + p' \tag{4.1.4}$$

Inserting (4.1.3) into the continuity equation (4.1.1) and time averaging gives the resulting continuity equation for the mean velocity in equation (4.1.5). By inserting (4.1.3) and (4.1.4) into the Navier-Stokes equations (4.1.2), and time averaging the result, we get the time averaged Navier-Stokes equations for turbulent flow (4.1.6). Hence, equation (4.1.1) and (4.1.2) has been transformed into,

$$\frac{\partial \overline{u}_j}{\partial x_j} = 0 \tag{4.1.5}$$

$$\frac{\partial \overline{u}_i}{\partial t} + \frac{\partial(\overline{u}_i\overline{u}_j)}{\partial x_j} = -\frac{1}{\rho}\frac{\partial \overline{p}}{\partial x_i} + \frac{\partial}{\partial x_j}\left(\nu\left[\frac{\partial \overline{u}_i}{\partial x_j} + \frac{\partial \overline{u}_j}{\partial x_i}\right] - \overline{u_i'u_j'}\right) \tag{4.1.6}$$

Equation (4.1.6) is called the Reynolds-Averaged Navier-Stokes (RANS) equations. The last term in (4.1.6) is important, and is included in the stress term as an addition to the viscous stress. It is called the Reynolds Stress and often denoted as $\tau_{ij} = -\overline{u_i' u_j'}$.

There is no natural way of calculating the Reynolds Stress, but one way to solve it is through the use of the Boussinesq approximation,

$$\tau_{ij} = -\overline{u_i' u_j'} = \nu_t \left(\frac{\partial \overline{u}_i}{\partial x_j} + \frac{\partial \overline{u}_j}{\partial x_i} \right) - \frac{2}{3} k \delta_{ij}. \tag{4.1.7}$$

In equation (4.1.7), ν_t is called the turbulent eddy viscosity, k is the turbulent kinetic energy defined as $k = \frac{1}{2}(\overline{u_i' u_i'})$ and δ_{ij} is the Kronecker delta. Now the problem has been reduced from modelling the Reynolds stress to determining the eddy viscosity, ν_t. Note that the eddy viscosity is not a physical value, only a way of approximating the Reynolds stress.

The last term of equation (4.1.7) is included to ensure that the normal turbulent stresses indeed becomes $k = \frac{1}{2}(\overline{u_i' u_i'})$. In equation (4.1.6), we are only interested in the pressure gradient and not the pressure itself. Because of this the last term of (4.1.7) can be added to the pressure. Therefore $\overline{p}$ is redefined as $\overline{p} = \overline{p}_n + (2/3)k$ where $\overline{p}_n$ is the mean pressure in equation (4.1.6). The substitution of (4.1.7) into (4.1.6) then becomes

$$\frac{\partial \overline{u}_i}{\partial t} + \frac{\partial (\overline{u}_i \overline{u}_j)}{\partial x_j} = -\frac{1}{\rho} \frac{\partial \overline{p}}{\partial x_i} + \frac{\partial}{\partial x_j} \left((\nu + \nu_t) \left[\frac{\partial \overline{u}_i}{\partial x_j} + \frac{\partial \overline{u}_j}{\partial x_i} \right] \right) \tag{4.1.8}$$

Because the laminar viscosity normally is much smaller than the turbulent eddy viscosity, it is often neglected, giving the following final expression for the time averaged momentum equation for turbulent flow

$$\frac{\partial \overline{u}_i}{\partial t} + \frac{\partial (\overline{u}_i \overline{u}_j)}{\partial x_j} = -\frac{\partial \overline{p}}{\partial x_i} + \frac{\partial}{\partial x_j} \left(\nu_t \left[\frac{\partial \overline{u}_i}{\partial x_j} + \frac{\partial \overline{u}_j}{\partial x_i} \right] \right). \tag{4.1.9}$$

However, we are left with a new unknown, namely the turbulent eddy viscosity ν_t. As a response, different turbulence models have been created for the purpose of solving for this unknown.

4.2 Turbulence models and solvers

Note that not all turbulence models are based on the Boussinesq approximation in (4.1.7). Therefore, not all of them are handling the closure problem with finding an estimate for the eddy viscosity, ν_t. However, these are often considered to be the simplest models, and to give the overall best accuracy to numerical cost ratio for most modelling purposes.

The most acknowledged perception of the eddy viscosity is that it is the product of a length scale l_e and a velocity scale V_e of the turbulent eddies within the flow. Hence,

$$\nu_t = l_e V_e \tag{4.2.1}$$

There are several ways of defining the velocity and length scale. The simplest way is to assume they are constant, hence ν_t is constant. A more applicable method is to assume that the velocity scale is changing over the depth while the length scale remains constant. This is the basics of what is referred to as the *mixing length* model. If the formulation of the turbulent velocity or length scale requires no additional conservation equations besides the continuity and RANS equations, then they are called zero equation models.

The turbulent velocity scale is often characterised using the turbulent kinetic energy k. This parameter has its own conservation equation. If the turbulent length scale is kept constant, the model is now called a one-equation model. A well known one-equation model is the *Spalart-Allmaras* model designed for aerodynamic flows.

The most accurate formulation of the eddy viscosity is to use the conservation equation for the turbulent kinetic energy, and couple it with a conservation equation for the dissipation of turbulent kinetic energy. Now the model is called a two-equation model because ν_t is dependent on two conservation equations. The most known two-equation models are probably the k-ε and k-ω models, where the k-ε is the one used for this study.

As stated, it is also possible to solve the RANS equations without using the Boussinesq approximation. The Reynolds Stress Transport models is based on solving conservation equations for the Reynolds Stresses directly. However, this is more complex than the eddy viscosity models.

The RANS equations are themselves simplifications. It is possible to solve the Navier-Stokes equations without time averaging them first. The method is then called DNS (Direct Numerical Simulation) and is done by solving the fluctuating velocity part of (4.1.3) instead of removing it by temporal averaging. This is not a turbulence model as the turbulence is actually being solved. However, in order to capture the small velocity fluctuations in the flow, this method requires a very dense grid of computational cells, and are therefore computationally expensive.

A number of hybrid methods have been developed from the DNS approach. LES (Large Eddy Simulation) is a growing approach where the requirement of a very dense grid of computational cells is avoided by only using DNS on the flow where the grid can support it. The model then uses the RANS equations for the fluctuations that are too small to be captured by the main grid. This is still an expensive approach, but less expensive than pure DNS.

A hybrid method of the LES is the DES (Detached Eddy Simulation). This approach uses LES as the standard solver, but is pre-modelled to use the RANS equations near walls or other regions where the general boundary layer is assumed to be known. There are two popular extensions of this model, namely the DDES (Delayed Detached Eddy Simulation) and the IDDES (Improved Delayed Detached Eddy Simulation). The main difference is the handling of the LES/RANS transitions.

4.3 k-ε model

In this study the k-ε model will be used to provide the closure for the RANS equations. There are several variations to this model, but the one used in this study is the standard high Reynolds number version presented in Launder and Spalding (1974). It evolves around the Boussinesq approximation, and is a two equation model in the sense that it provides conservation equations for both the turbulent kinetic energy k and the dissipation of turbulent kinetic energy, denoted ε. The turbulent kinetic energy and the dissipation is coupled to the eddy viscosity ν_t through the the relation,

$$\nu_t = C_\mu \frac{k^2}{\varepsilon} \tag{4.3.1}$$

where C_μ normally is considered a constant.

The conservation equation for the turbulent kinetic energy, k, can be derived from the Navier-Stokes equations. First substituting (4.1.3) into (4.1.2), and then subtracting with the time averaged Navier-Stokes equations (4.1.6), gives a conservation equation for the turbulent fluctuations u_i'. Multiplying with u_i', and time averaging, gives the conservation equation for the turbulent kinetic energy k where $k = \frac{1}{2}\overline{u_i' u_i'}$. The complete derivation is found in Hinze (1975). The conservation equation for ε is not strictly mathematical. The following conservation equations for k and ε are presented as in Launder and Spalding (1974),

$$\frac{\partial k}{\partial t} + \overline{u}_j \frac{\partial k}{\partial x_j} = \frac{\partial}{\partial x_j}\left(\frac{\nu_t}{\sigma_k}\frac{\partial k}{\partial x_j}\right) + \nu_t\left(\frac{\partial \overline{u}_i}{\partial x_j} + \frac{\partial \overline{u}_j}{\partial x_i}\right)\frac{\partial \overline{u}_i}{\partial x_j} - \varepsilon \tag{4.3.2}$$

$$\frac{\partial \varepsilon}{\partial t} + \overline{u}_j \frac{\partial \varepsilon}{\partial x_j} = \frac{\partial}{\partial x_j}\left(\frac{\nu_t}{\sigma_\varepsilon}\frac{\partial \varepsilon}{\partial x_j}\right) + C_{\varepsilon 1}\frac{\varepsilon}{k}\nu_t\left(\frac{\partial \overline{u}_i}{\partial x_j} + \frac{\partial \overline{u}_j}{\partial x_i}\right)\frac{\partial \overline{u}_i}{\partial x_j} - C_{\varepsilon 2}\frac{\varepsilon^2}{k} \tag{4.3.3}$$

where,

$$(C_\mu, C_{\varepsilon 1}, C_{\varepsilon 2}, \sigma_k, \sigma_\varepsilon) = (0.09, 1.44, 1.92, 1.00, 1.30), \tag{4.3.4}$$

are standard constants (Rodi (1993), Launder and Spalding (1974)). From the left, the terms in equation (4.3.2) and (4.3.3) are the instantaneous change of the quantity, the convection term, the transport term, the production term and the dissipation term.

4.4 Wall functions

In turbulent flows over smooth walls or surfaces, the boundary layer can be said to be decomposed into four regions. Closest to the wall the flow will be laminar, and viscous effects will dominate the flow characteristics. This layer is called the *viscous sublayer*. A small distance further from the wall, turbulent effects will be present, but viscous

effects are still dominant. This is the *buffer layer*. After the buffer layer, turbulent effects becomes dominant over the viscous ones and we call the layer for the *overlap layer*. Then, far enough from the wall the flow will be more or less unaffected by the presence of the wall, and we move into the fully turbulent region of the flow. The different regions are illustrated in figure 4.1.

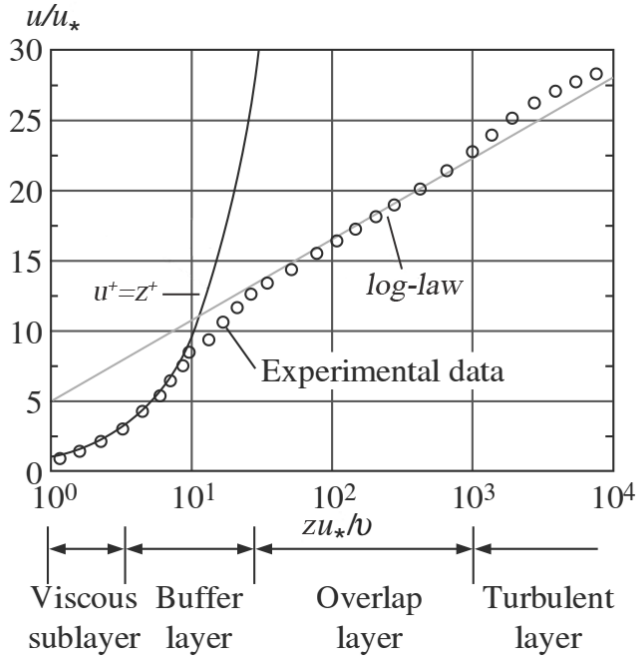

Figure 4.1: Log-plot of $u^+ = u/u_*$ as a function of $z^+ = zu_*/\nu$. The *law of the wall* ($u^+ = z^+$) and the *log-law* are plotted against experimental data to show their regions of validity. (Cengel and Cimbala (2010))

The standard k-ε model, as presented in (4.3.2) and (4.3.3), is only valid for fully turbulent flow, meaning high Reynolds numbers. The presence of a smooth no-slip wall introduces local low Reynolds number regions close to the wall in which the standard k-ε is not valid due to the dominating viscous effects. The solution is to introduce so called *wall functions*. These are semi-empirical formulas that give an approximation of the boundary layer where the viscous effects are present, without the need to numerically solve these regions. This is beneficial both because the solution becomes more accurate due to the k-ε equations actually being valid, but also because it saves computational costs due to less grid refinement is needed near the wall (Rodi (1993)).

The normal way wall functions are implemented is by utilizing the empirical expression for the overlap layer. This formula is found from experiments and is called *the logarithmic law* or simply the *log-law*. Its general form is shown in (4.4.1) as portrayed in Rodi (1993),

$$u(z) = \frac{u_*}{\kappa} ln(Ez^+), \tag{4.4.1}$$

where E is a roughness parameter and κ is the von Karman constant assigned the value

of 0.4 (Holmedal and Myrhaug (2013)). The nondimensional first cell thickness is given as $z^+ = zu_*/\nu$, and u_* is called the friction velocity, defined as

$$u_* = \sqrt{\frac{\tau_w}{\rho}}, \tag{4.4.2}$$

where τ_w is the wall shear stress. Because the friction velocity u_* is a function of the wall shear stress, equation (4.4.1) has coupled the fluid velocity outside the viscous sublayer to the laminar shear stress τ_w at the wall.

For a smooth surface the roughness parameter can be set as $E = 9$ (Rodi (1993)). For a hydraulically rough surface, the roughness parameter can be approximated as $E = 30\nu/u_* k_n$ (López and García (2001)). The latter expression substituted into equation (4.4.1) gives,

$$u(z) = \frac{u_*}{\kappa} ln(\frac{z}{z_0}). \tag{4.4.3}$$

where $z_0 = k_n/30$ is called the *bottom roughness* or *bed roughness*, and k_n is the Nikuradse roughness which is related to the sand grain diameter of the surface.

Because the ocean sea bed is rough, the rough log-law in (4.4.3) will be used to model the tidal flow. If nothing else is specified the bottom roughness is $z_0 = 0.0006\, cm$.

For the application of the k-ε-model, Rodi (1993) proposed the following initial conditions for k and ε at a wall or surface,

$$k = \frac{u_*^2}{\sqrt{C_\mu}} \tag{4.4.4}$$

$$\varepsilon = C_\mu^{3/4} \frac{k^{3/2}}{\kappa z} \tag{4.4.5}$$

From initial guesses of the velocity at the first node (node 1) at distance z from the surface, the wall function in equation (4.4.3) can be rearranged to explicitly give the friction velocity u_*. By substituting the friction velocity into equation (4.4.4) and (4.4.5), the bed roughness z_0 will be directly coupled to the turbulence generation and dissipation at node 1. Hence, the initial turbulence generation at the first computational cell will be coupled to the surface roughness without actually resolving that part of the boundary layer.

4.5 Wave-current damping

Waves are often present when considering tidal currents. The orbital motion of the water particles under the waves will induce an additional damping on the current velocity. The simplest way of accounting for this additional wave induced damping is to incorporate it

into the current through the bed roughness z_0 in equation (4.4.3). Figure 4.2 illustrates the relation between the mean velocity profile of a pure current flow and a current-wave flow, and how they can be connected to the bed roughness. Instead of the actual bed roughness z_0, the current-wave flow can be modelled using the fictive bed roughness z_a.

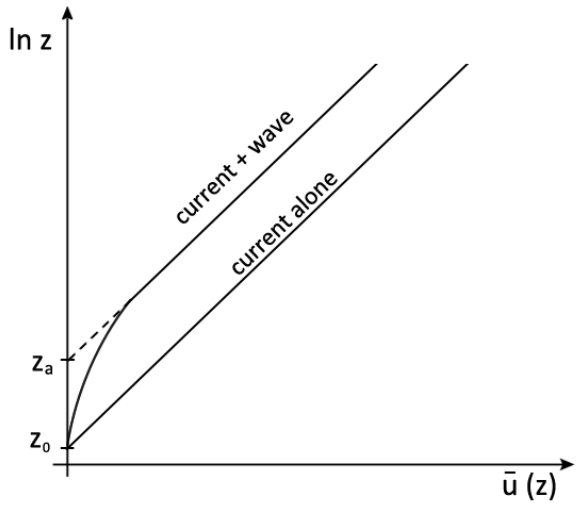

Figure 4.2: Illustration of the relation between a pure current and a current-wave flow with regards to the bed roughness. (Reproduced from Nielsen (1992))

5 Canopy flow

In order to model tidal flow over submerged aquatic vegetation, understanding how the canopy effects the mean flow mechanisms must be accomplished. Both canopy density, canopy height to depth ratio, the shape of the plants, and their stiffness affects the flow in different ways. This chapter will give a brief overview of these effects and the physical mechanisms they induce onto the mean flow.

The theory explained in this chapter is primarily based on the extensive overview of canopy related flow given in Nepf (2012a) and Nepf (2012b).

5.1 Canopy parameters

Some parameters are frequently used in the terminology of canopy flow. The plant frontal area per canopy volume, a, is expressed as the stem diameter d over the square of the averaged distance ΔS between each stem,

$$a = \frac{d}{\Delta S^2}, \tag{5.1.1}$$

with unit $[1/m]$. The representative canopy diameter d will normally vary with the height of real life aquatic canopies. Hence, so will the frontal area per volume, a. Integrating a over the canopy height gives the frontal area per bed area which is a non-dimensional value for the canopy density. It is often referred to as the roughness density (Nepf (2012a)),

$$\lambda_f = \int_0^h a dz \tag{5.1.2}$$

where h is the canopy height. Hence, for a canopy represented by rigid circular cylinders, the canopy density becomes $\lambda_f = ah$. Another parameter frequently used by Nepf (2012a) is the solid volume fraction ϕ, defined as the cross sectional area of the plant stem divided by the bed area ΔS^2.

5.2 Emergent canopies

Emergent canopies are canopies that penetrates the water surface, and therefore covers the entire depth of water column. These types of canopies introduce two additional effects on the mean flow. Firstly, they introduce a drag force on the flow, hence damping it throughout the whole depth. Secondly, energy is taken from the mean flow and transformed into turbulence in the wakes behind each individual plant stem. The length scale of this generated turbulence will depend on the density of the canopy. If the averaged spacing between the plant stems (ΔS) are larger than the stem diameter (d), then the

wake generated turbulence will be of the order of the stem diameter. However, for canopies with density causing the averaged spacing between the stems to be smaller than the stem diameter, the turbulence length scale will be of the order of the averaged stem spacing ΔS (Nepf (2012a)).

Because the canopy is emergent, all turbulent eddies that normally would exist in a turbulent flow, are rescaled into length scales corresponding to either d or ΔS. If the water depth is large compared to d or ΔS this will result in an negligible vertical transport of turbulence due to the turbulent length scale being inferior to the water depth.

For most cases, the averaged stem spacing is larger than the diameter d. The length-scale of the wake-generated turbulence is therefore of the order of the stems, and commonly referred to as *stem-scale* turbulence. In this study, all wake-generated turbulence is referred to as stem-scale turbulence.

5.3 Submerged canopies

Submerged canopies are canopies where the plant height is smaller than the water depth, $H > h$. It is normal to distinguish between different H/h-ratios. In addition to the emergent condition $H/h = 1$, the submerged condition is described as shallow submerged if $H/h < 5$, and deeply submerged if $H/h < 10$. The latter is normally the case for flow over terrestrial canopies. Due to lighting conditions most aquatic canopies are found within the shallow submerged region. The rest of this chapter will therefore focus on the effects occurring in this region.

The main difference between the flow through an emergent and a shallow submerged canopy is what happens in the transition between the canopy and the undisturbed flow above the canopy. There will be two separate effects depending on the relative density of the canopy. If the canopy is sparse ($\lambda_f << 0.1$), Nepf (2012a) states that the bed friction is larger than the canopy drag, and the presence of the canopy can be included in the bed roughness parameter z_0 in equation (4.4.3). The boundary layer will therefore follow the normal logarithmic profile as shown in figure 5.1a.

If the canopy is sufficiently dense ($\lambda_f >> 0.1$), the canopy drag will be significantly larger than the bed friction, and the inclusion of the canopy drag into the bed roughness will be erroneous. In this case, the additional drag imposed on the flow by the canopy leads to the generation of a shear layer at the top of the canopy. The shear layer has an inflection point that leads to flow instabilities and vortex generation near the top of the canopy. There is consensus in the meteorological and water research community to draw the analogy between the interaction of in-canopy flow and above-canopy flow with that of a mixing layer. Hence, the occurring flow instabilities are commonly referred to as Kelvin-Helmholtz instabilities. The vortices generated are referred to as shear-scale or *canopy-scale* vortices, and for the case of shallow submergence these vortices are normally dominating the vertical transport of turbulence between the canopy and the unobstructed flow. Contrary to the vortex generation in a mixing layer, the canopy-scale vortices quickly reaches a finite size as the additional energy going into the vortices through vortex pairing equals the energy being taken away by the canopy drag (Ghisalberti and Nepf (2004)).

The length-scale of these vortices will be further dependent on the canopy density. Nepf (2012a) states that if $0.1 < C_D ah < 0.23$ (with $C_D \approx 1$), the canopy-scale vortices penetrates to the sea bed as shown in figure 5.1b. This is called the transitional region, and if δ_e is the distance the vortex penetrates into the canopy, then $\delta_e = h$. For denser canopies ($C_D ah > 0.23$) the canopy drag will absorb too much energy from the vortices hence preventing them from reaching the sea bed. In this case they will penetrate a distance $\delta_e < h$ into the canopy as shown in figure 5.1c. The distance to the surface will also be a limiting factor for the generation of canopy-scale vortices. Nepf and Vivoni (2000) concluded that if $H/h < 2$, the generation of canopy-scale vortices would, to some degree, be restricted by the free surface.

The density limits discussed, and depicted in figure 5.1, are crude. Nepf (2012a) states, from earlier findings, that a pronounced shear layer occurs for $C_D ah > 0.1$ ($C_D \approx 1$), while no shear layer is observed if $C_D ah < 0.04$.

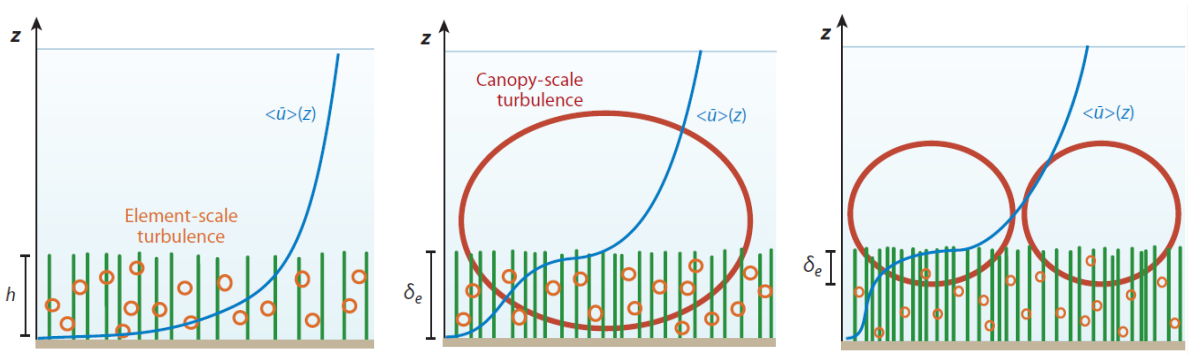

(a) Sparse, $ah << 0.1$ (b) Transitional, $ah \approx 0.1$ (c) Dense, $ah >> 0.1$

Figure 5.1: Illustration of how the canopy density effects the flow pattern (Nepf (2012a)).

As mentioned, the canopy-scale vortices will be dominating the vertical turbulent transport over their range in the water column. In the case of $\delta_e < h$ the canopy-scale vortices will separate the canopy into two distinct layers. The layer defined by the region δ_e will have a large vertical turbulent transport due to the canopy-scale vortices stirring the flow. The layer closest to the sea bed will be dominated by the same stem-scale turbulence as for the emergent canopy, hence causing a limited amount of transport. Ghisalberti and Nepf (2006) named the first zone the *exchange zone* and the latter the *wake zone*. From an ecology point of view, both zones are important as the exchange zone provides rapid water renewal and removal of contaminant, while the wake zone has the ability to trap nutrients.

As pointed out by Nepf (2012a), what separates the flow through an aquatic canopy from the flow through a terrestrial (deeply submerged) canopy is that the large H/h-ratio of the terrestrial canopy results in the regular boundary-layer turbulence to out-scale the canopy-scaled turbulence. In an aquatic canopy the limited H/h-ratio prevents the growth and extend of the boundary layer between the canopy and the free surface, hence making the canopy-scaled vortices the dominant ones. Figure 5.2 illustrates the different turbulence

scales for flow over a dense canopy. Larger H/h-ratios result in more dominant boundary layer turbulence. However, for $H/h < 5$, as is often the case for aquatic vegetation, the canopy-scale vortices will be the most dominant ones. Note that the boundary layer turbulence generated by the sea bed normally is negligible in comparison with the wake-scale turbulence (Nepf et al. (1997)).

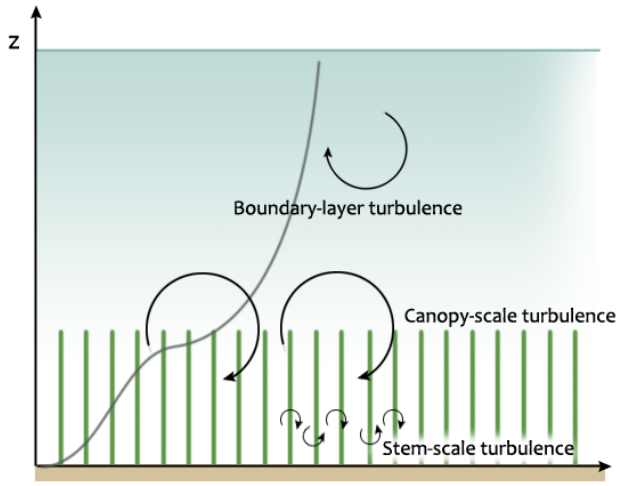

Figure 5.2: Illustration of the different vortex-scales important for canopy flow. Note that the boundary layer turbulence generated by the sea bed normally is negligible.

5.4 Flexible canopies

The stiffness of an aquatic plant is a function of both its rigidity and its buoyancy. Important to consider is also that many aquatic species have entrapped air pockets as part of their structure, hence contributing largely to its buoyancy. Nepf and Vivoni (2000) divides the effect of canopy flexibility into four regimes of motion corresponding to increasing flexibility, namely erect, gently swaying, strong coherent swaying and prone. The flow mechanisms described in this chapter applies only to the rigid and gently swaying state. The strong coherent swaying and pronated state will have additional flow mechanisms (Nepf and Vivoni (2000)).

The strong coherent swaying is a phenomenon commonly referred to a *monami* (Nepf (2012a)). It occurs if the instantaneous force from the canopy-scale vortices, penetrating into the canopy, overcomes the stiffness of the plants. As opposed to unobstructed vortices, the canopy-scale vortices will have a decrease in rotational speed due to the canopy drag. This causes their centre of rotation to be deflected upwards in regards to the top of the canopy. Coupled with the decrease in rotational speed, this gives the canopy-scale vortices a significant translational speed along the top of the canopy, forcing the canopy to deflect forward and down. The propagation of the canopy-scale vortices then causes the wave-like motion of the canopy, known as monami.

The monami effects the flow in terms of a larger penetration depth into the canopy at intervals corresponding to when the canopy is displaced the most (Ghisalberti and Nepf (2002)). However, it decreases the turbulent vertical transport through the canopy compared to if the canopy was rigid (Ghisalberti and Nepf (2006)).

6 Spatial averaging

As mentioned in the introduction, the governing equations must be spatially averaged in order to account for the heterogeneity in the flow due to the geometry of the vegetation. Wilson and Shaw (1977) were supposedly the first to systematically and thoroughly performing this averaging process.

They proposed two different methods to performe this averaging. The first method (referred to as scheme I) involved spatially averaging over a wide enough area so that the mean flow became independent of both the canopy geometry and the temporal fluctuations of the turbulence. The second method (scheme II) involved first taking the temporal average to make the mean flow independent of the temporal fluctuations (same procedure as for deriving the RANS equations in section 4.1), and then performing a spatial average to account for the canopy geometry. They concluded that the two procedures gave equal results. However, Raupach and Shaw (1982) argued that this wasn't necessarily the case as the second averaging scheme produces additional terms that should be given some more attention.

For the spatial averaging in scheme I, the velocity and pressure are decomposed in a similar manner as the temporal decomposition in equation (4.1.3) and (4.1.4), namely by a mean and a fluctuating component,

$$u_i = \langle u_i \rangle + u_i'' \tag{6.0.1}$$

$$p = \langle p \rangle + p'' \tag{6.0.2}$$

In equation (6.0.1) and (6.0.2), angle brackets represents the spatially mean value, and the double primes represents how the velocity and pressure fluctuates with respect to the horizontal plane. Substitution of equation (6.0.1) and (6.0.2) into the Navier-Stokes equations, and spatially averaging over a large enough area gives the resulting momentum equation under scheme I.

The momentum equation under scheme II is derived by first taking the temporal averaged to obtain equation (4.1.6). The time averaged mean component of the velocity and pressure are then decomposed into a spatial mean and a spatial fluctuating component as for scheme I, hence

$$\overline{u}_i = \langle \overline{u}_i \rangle + \overline{u}_i'' \tag{6.0.3}$$

$$\overline{p} = \langle \overline{p} \rangle + \overline{p}'' \tag{6.0.4}$$

Equation (6.0.3) and (6.0.4) are then substituted into equation (4.1.6), and spatially averaging this equation will produce the momentum equation under scheme II.

The spatial averaging in full will not be reviewed here as it is fairly complicated and lengthy. The resulting equations from both schemes are given in appendix A as a brief overview of their general shape. For a full overview of the equations, and some of the things to be aware of when deriving them, the reader is advised to study the papers of Wilson and Shaw (1977) and Raupach and Shaw (1982). Their papers are fully dedicated on explaining the complete derived equations and part of the procedure needed to derive them.

This chapter is a coarse overview of the most important effects from the spatial averaging process that are directly coupled with how the momentum and k-ε equations are modified in order to account for the vegetation.

6.1 Momentum equation

As stated, Raupach and Shaw (1982) argued that the two different averaging schemes did not produce the exact same results. Scheme II produces what Raupach and Shaw (1982) refer to as *dispersive* fluxes $\langle \overline{u}_i'' \overline{u}_j'' \rangle$. These are additional stress terms that result from the correlation between the time-averaged and spatially averaged velocity. According to Raupach and Shaw (1982) these dispersive fluxes were more than just mathematical byproducts in spite of that they, up to the release of their paper, had not been directly measured in experiments. Besides the dispersive fluxes, the results from scheme I and scheme II were the same.

Poggi et al. (2004) performed flume experiments using rigid submerged cylinders, and managed to measure these dispersive fluxes. The results were compared with the Reynolds stress to determine the relative importance between the two, and was repeated for several cylinder densities. Poggi et al. (2004) found that the dispersive fluxes are less than 10% of the Reynolds stress for dense canopies ($ah > 0.1$), but reaches 35% for the most sparse canopy tested ($ah = 0.03$). Regardless of density, the dispersive fluxes are only significant in the lower portion of the canopy ($z/h < 0.5$). For ($z/h > 0.5$) they are significantly smaller and have opposite signs compared to the measured Reynolds stress. If this is a result of the canopy-scale vortices was not commented on in the paper. However, according to Nepf (2012a), the flow follows a logarithmic boundary layer profile if $C_D ah < 0.04$, ($C_D \approx 1$). Hence, no canopy-scale vortices can occur at these low densities.

The general conclusion in the literature appears to be that the dispersive fluxes are negligible for dense canopies ($ah > 0.1$).

In addition to the dispersive stresses, what Raupach and Shaw (1982) found was that the spatial averaging of the momentum equations generated two additional terms, namely a viscous drag term

$$f_V = \nu \langle \nabla^2 \overline{u}'' \rangle, \tag{6.1.1}$$

and a pressure drag term

$$f_D = \frac{1}{\rho}\left\langle \frac{\partial \overline{p}''}{\partial x} \right\rangle, \tag{6.1.2}$$

where $\overline{u}''$ and $\overline{p}''$ are the spatial fluctuation of the time averaged velocity and pressure, respectively. As stated, overbars represent the temporal mean of quantities while angle brackets represents the spatial mean. ν, ρ and ∇ are the laminar viscosity, water density and Laplace operator, respectively. Both terms removes energy from the momentum equations. The terminology in equation (6.1.1) and (6.1.2), and the rest of the equations presented in this chapter, are adopted from averaged scheme II.

The viscous term is assumed neglectable compared to the form drag. The form drag is widely assumed to follow the quadratic drag law, hence

$$f_D = \frac{1}{\rho}\left\langle \frac{\partial \overline{p}''}{\partial x} \right\rangle \approx \frac{1}{2} C_D a \langle \overline{u}_i \rangle^2 \tag{6.1.3}$$

where C_D is the drag coefficient representing the averaged form drag of the canopy, and a is the frontal area per volume of the canopy, given in equation (5.1.1).

The use of a quadratic drag law can be questioned when applied to flexible vegetation. The displacement of the blades due to the current will lead to both a reduced frontal area of the canopy, and most probably a more streamlined configuration of the plants. Several authors have therefore proposed having the drag force f_D vary with the velocity to the power of a parameter depending on the flexibility, rather than the standard quadratic law (Nepf (2012a)). However, Nepf (2012a) states that the increased accuracy gained from doing so often will be overshadowed by the uncertainty of both the drag coefficient C_D and the frontal area per volume, a, for a real life canopy.

6.2 TKE equation

As discussed in chapter 5, the interaction between the mean flow and the canopy will produce additional turbulent kinetic energy (TKE). Only accounting for the vegetation in the momentum equations will therefore lead to erroneous results. Wilson and Shaw (1977) and Raupach and Shaw (1982) both derived the TKE equations using the same schemes as for the momentum equations (scheme I and scheme II).

Similar to the derivation of the momentum equations, Scheme II produces dispersive terms in the TKE equation. However, the most interesting addition to the TKE equation is an additional turbulence production term. This production term corresponds to the additional turbulence generated in the stem wakes as discussed in section 5.2. In order for scheme I and scheme II to result in the same expression for the wake production term, a couple of assumptions must be made. First, the dispersive terms must be neglected. Secondly, the turbulent length scales created by the stem wakes must be larger than the Kolmogorov microscale. This is the smallest turbulent length scale that can exist in a

flow before the eddy is dissipated to heat. Physically, this means that no turbulent kinetic energy is dissipated directly to heat trough viscous drag.

Under these two assumptions, the additional TKE production terms from both schemes coincide. Under the terminology of scheme II it becomes

$$P_w = \frac{1}{\rho}\langle \overline{u}_i \rangle \left\langle \frac{\partial \overline{p}''}{\partial x} \right\rangle, \tag{6.2.1}$$

were $\langle \overline{u}_i \rangle$ is the spatial mean of the temporal mean velocity, and $\langle \partial \overline{p}''/\partial x \rangle$ is the spatial mean of the spatial fluctuating pressure gradient of the temporal mean pressure. Applying the approximation in equation (6.1.3), the additional TKE production can be expressed as

$$P_w = \frac{1}{\rho}\langle \overline{u}_i \rangle \left\langle \frac{\partial \overline{p}''}{\partial x} \right\rangle \approx \frac{1}{2} C_D a \langle \overline{u}_i \rangle^3 = f_D \langle \overline{u}_i \rangle, \tag{6.2.2}$$

where f_D is the canopy form drag given in equation (6.1.3). Because this is the extra turbulence generated in the wakes behind individual stems, it is commonly referred to as the *wake-production* term.

López and García (2001) argues that the assumption of no heat dissipation due to viscous drag does not always hold. Nepf and Vivoni (2000) states that it is reasonable to fully exclude the dissipation from viscous drag if the Reynolds number is $Re = dU/\nu > 200$, with d as the stem diameter of blade length and U as the inflow velocity. Below this Reynolds number the approximation in (6.2.2) will overpredict the TKE generation from the stem wakes.

Instead of denying the validity of equation (6.2.1) if the viscous dissipation is not negligible, López and García (2001) states that the problem can be sorted through the inclusion of a coefficient to represent the amount of energy that is actually being transformed from the mean flow into TKE. Hence

$$P_w = C_{fk} f_D \langle \overline{u}_i \rangle, \tag{6.2.3}$$

where C_{fk} is the coefficient representing the amount of work, generated by the form drag against the flow, that is transformed into TKE. $C_{fk} = 1$ then means that all the work created by the flow against the form drag of the canopy is transferred into turbulent kinetic energy. The inclusion of this coefficient is not something new, as it has been done previously by for instance Shimizu and Tsujimoto (1994). However, López and García (2001) coupled it to the averaging schemes and gave it a physical meaning.

For the modelling of vegetation as circular cylinders, López and García (2001) states that $C_{fk} = 1$ in general is a valid approximation.

6.3 Dissipation equation

The dissipation of the turbulent kinetic energy is not described by either Wilson and Shaw (1977) or Raupach and Shaw (1982), as they did not study the k-ε model in particular. Because of the additional TKE produced by the wake-scale turbulence, the conservation of dissipation of TKE, ε, must be modifies as well. López and García (2001) used the following expression to model the additional dissipation of the wake-scale turbulent kinetic energy,

$$D_w = C_{\varepsilon 1}\frac{\varepsilon}{k}C_{f\varepsilon}f_D\langle\overline{u}_i\rangle \tag{6.3.1}$$

where k is the turbulent kinetic energy, ε is the dissipation of turbulent kinetic energy, and $C_{\varepsilon 1}$ is the standard coefficient given in equation (4.3.4). $C_{f\varepsilon}$ is a new coefficient that must be related to the amount of wake-produced TKE. Therefore it must be related to C_{fk}. López and García (2001) coupled these two coefficients by assuming a state of steady horizontal flow through a canopy consisting of infinitely long vertical cylinders (similar to emergent vegetation over a large water depth). All transport terms can be approximated to zero as discussed in section 5.2, therefore reducing the TKE equation to an equilibrium between the wake-generated turbulence and the dissipation,

$$C_{fk}f_D\langle\overline{u}_i\rangle = \varepsilon \tag{6.3.2}$$

Correspondingly, the ε-equation would be an equilibrium between the additional production rate of dissipation due to the wake-scale turbulence and the viscous dissipation to heat,

$$C_{\varepsilon 1}\frac{\varepsilon}{k}C_{f\varepsilon}f_D\langle\overline{u}_i\rangle = C_{\varepsilon 2}\frac{\varepsilon^2}{k} \tag{6.3.3}$$

Substitution of equation (6.3.2) into equation (6.3.3) gives the following expression for $C_{f\varepsilon}$,

$$C_{f\varepsilon} = \frac{C_{\varepsilon 2}}{C_{\varepsilon 1}}C_{fk} \tag{6.3.4}$$

Assuming $C_{fk} = 1$, and applying the standard coefficients in equation (4.3.4), López and García (2001) stated that $C_{f\varepsilon} = 1.33$ is a reasonable value to use for the additional coefficient in equation (6.3.1).

6.4 Limitations

The most obvious limitation of the terms derived to account for the vegetation is that they only consider the turbulence generated from the stem wakes. The canopy-scale vortices

are therefore not accounted for in the conservation equations for either the momentum or the TKE. This is of concern since the canopy-scale vortices will dominate the turbulent transport over the smaller stem-scale turbulence (see section 5.3).

Ghisalberti and Nepf (2004) derived their own numerical model accounting for the canopy-scale vortices. They used a one-equation closure scheme, hence only considering the conservation equation for momentum and TKE. The form drag in equation (6.1.3) is incorporated into their momentum equation as it would for a normal k-ε model. However, by confining their model to apply only within the height-span of a canopy-scale vortex, they neglected the general TKE production and the TKE production from the stem wakes. By also neglecting the viscous dissipation and the transport terms, they end up with a conservation between the canopy-scale TKE production, expressed using the Reynolds stress, and the dissipation as the canopy-scale turbulence is broken into wake-scale turbulence with the canopy. They obtained good results, however the limited range for which it is valid, and its underlying assumptions, are not compatible with the k-ε model.

Uittenbogaard (2003) utilized a k-ε model, but modified the dissipation term (6.3.1) in order to account for the canopy-scale vortices. The modified equations are presented as in Baptist et al. (2007) and Dijkstra and Uittenbogaard (2010). Instead of the additional dissipation term in equation (6.3.1), he defined

$$D_w = \frac{1}{\tau_{eff}} C_{\varepsilon 2} f_D \langle \overline{u}_i \rangle \tag{6.4.1}$$

where τ_{eff} is the smaller τ_{int} and τ_{geom}, given as

$$\tau_{int} = \frac{k}{\varepsilon}, \quad \tau_{geom} = \left(\frac{L_p^2}{C_\mu^2 f_D \langle \overline{u}_i \rangle} \right)^{1/3} \tag{6.4.2}$$

and where,

$$L_p = C_1 \left(\frac{1 - Ap}{n} \right)^{1/2}. \tag{6.4.3}$$

τ_{int} and τ_{geom} are referred to as the intrinsic and geometrical times scale, respectively. L_p is defined as the available length scale within the canopy. Hence, the geometrical time scale is connected with the geometrical length scale of the canopy. The analogy is that when canopy-scale vortices penetrates into the canopy they are forced into the smaller wake-scale turbulence, and that the result is increased production of dissipation.

The rest of the terms in equation (6.4.1)–(6.4.3) are, $C_\mu = 0.09$, C_1 is a geomtery factor (=1 for cylinders), $n = a/d[1/m^2]$, and A_p is the same as the volume fraction ϕ defined in section 5.1.

Noting that $C_{\varepsilon 2} \approx C_{\varepsilon 1} C_{f\varepsilon}$ if $C_{f\varepsilon} = 1.33$, then $\tau_{eff} = \tau_{int}$ produces the same expression in (6.4.1) as equation (6.3.1). Although the purpose of this modification is justified, the origin and mathematical background for the equations are not thoroughly explained.

7 Numerical model

7.1 Governing equations

The model used in this study is a one dimensional finite difference model utilizing a staggered grid. The velocity components in the x and y direction are calculated at each node while the k and ε values are calculated between each node. The nodes are spaced in a logarithmic fashion throughout the water column with higher density closer to the bed in order to capture the boundary layer profile.

Utilizing that the length scales are far greater than the depth scales, a scaling analysis can be made. Equation (4.1.9) can be simplified into,

$$\frac{\partial u}{\partial t} + u\frac{\partial u}{\partial x} + v\frac{\partial u}{\partial y} = -\frac{1}{\rho}\frac{\partial p}{\partial x} + \frac{\partial}{\partial z}\left(\nu_t \frac{\partial u}{\partial z}\right) \tag{7.1.1}$$

$$\frac{\partial v}{\partial t} + u\frac{\partial v}{\partial x} + v\frac{\partial v}{\partial y} = -\frac{1}{\rho}\frac{\partial p}{\partial y} + \frac{\partial}{\partial z}\left(\nu_t \frac{\partial v}{\partial z}\right) \tag{7.1.2}$$

$$0 = \frac{\partial p}{\partial z} \tag{7.1.3}$$

This is called the boundary layer approximation. In addition, the Coriolis force must be incorporated for tidal flow. If the Rossby number is small enough (see section 2.1) the convection terms will be negligible compared to the Coriolis acceleration. From a modelling perspective this means that the momentum equations are reduced from being partial differential equations to ordinary differential equations, making them easier to solve.

In addition, the form drag expressed by the quadratic drag law in equation (6.1.3) is included. Hence, equation (7.1.1) and (7.1.2) can be written as

$$\frac{\partial u}{\partial t} = -\frac{1}{\rho}\frac{\partial p}{\partial x} + \frac{\partial}{\partial z}\left(\nu_t \frac{\partial u}{\partial z}\right) + fv - f_{Dx} \tag{7.1.4}$$

$$\frac{\partial v}{\partial t} = -\frac{1}{\rho}\frac{\partial p}{\partial x} + \frac{\partial}{\partial z}\left(\nu_t \frac{\partial v}{\partial z}\right) - fu - f_{Dy} \tag{7.1.5}$$

where fv is the component of the Coriolis force acting in x-direction and fu is the one acting in the y-direction. f_{Dx} and f_{Dy} are the direction specific form drag in x- and y-direction, respectively. Hence,

$$f_{Dx} = \frac{1}{2} C_D a u|u| \tag{7.1.6}$$

$$f_{Dy} = \frac{1}{2} C_D a v |v| \tag{7.1.7}$$

Performing a scaling analysis for the k and ε equation in (4.3.2) and (4.3.3), and including the additional wake production (6.2.3) and dissipation (6.3.1), they become

$$\frac{\partial k}{\partial t} = -\frac{\partial}{\partial z}\left(\frac{\nu_t}{\sigma_k}\frac{\partial k}{\partial z}\right) + \nu_t\left(\left(\frac{\partial u}{\partial z}\right)^2 + \left(\frac{\partial v}{\partial z}\right)^2\right) - \varepsilon + P_w \tag{7.1.8}$$

$$\frac{\partial \varepsilon}{\partial t} = -\frac{\partial}{\partial z}\left(\frac{\nu_t}{\sigma_\varepsilon}\frac{\partial \varepsilon}{\partial z}\right) + C_{\varepsilon 1}\frac{\varepsilon}{k}\nu_t\left(\left(\frac{\partial u}{\partial z}\right)^2 + \left(\frac{\partial v}{\partial z}\right)^2\right) - C_{\varepsilon 2}\frac{\varepsilon^2}{k} + D_w \tag{7.1.9}$$

where $(C_{\varepsilon 1}, C_{\varepsilon 2}, \sigma_k, \sigma_\varepsilon) = (1.44, 1.92, 1.00, 1.30)$, and P_w and D_w are expressed as

$$P_w = C_{fk}\frac{1}{2} C_D a |\mathbf{u}|^3 \tag{7.1.10}$$

$$D_w = C_{\varepsilon 1}\frac{\varepsilon}{k} C_{f\varepsilon}\frac{1}{2} C_D a |\mathbf{u}|^3 \tag{7.1.11}$$

Here, $\mathbf{u}$ is the resulting velocity vector (u, v).

The coefficients C_{fk} and $C_{f\varepsilon}$ are taken from López and García (2001) and has the value of 1 and 1.33, respectively (see section 6.2 and 6.3).

Above the canopy ($z > h$) the drag coefficient is defined zero, $C_D = 0$, hence reducing the momentum equations ((7.1.4), (7.1.5)) and the k-ε equations ((7.1.8), (7.1.9)) to what they would have been for an unobstructed tidal flow.

There is no separate equation for the pressure gradient in equation (7.1.4) and (7.1.5). However, by assuming that the upper part of the water column can be modelled as potential flow, the viscous term in equation (7.1.4) and (7.1.5) can be neglected. Hence, the following conservation equations arise

$$\frac{\partial u}{\partial t} = -\frac{1}{\rho}\frac{\partial p}{\partial x} + fv \tag{7.1.12}$$

$$\frac{\partial v}{\partial t} = -\frac{1}{\rho}\frac{\partial p}{\partial y} - fu \tag{7.1.13}$$

By using field measurements of the velocity time series, the pressure gradient for the upper part of the water column can be solved explicitly as,

$$-\frac{1}{\rho}\frac{\partial p}{\partial x} = \frac{\partial u_0}{\partial t} - fv_0 \tag{7.1.14}$$

$$-\frac{1}{\rho}\frac{\partial p}{\partial y} = \frac{\partial v_0}{\partial t} + f u_0 \tag{7.1.15}$$

where u_0 and v_0 are extrapolated from the time series at each given time t. And since the pressure gradient is constant in z-direction (7.1.3), the pressure gradients in equation (7.1.4) and (7.1.5) are known.

All pressure and velocity terms in equation (7.1.4) – (7.1.15) are averaged in both time and space.

7.2 Boundary conditions

At sea bed:

At the sea bed the log-law in equation 4.4.3 for a rough surface is used, hence

$$u(z) = \frac{u_*}{\kappa} ln(\frac{z}{z_0}), \tag{7.2.1}$$

For the modelling of tidal flow the bed roughness is set to $z_0 = 0.0006\, cm$.

The horizontal velocity components are zero due to the no-slip condition, hence

$$u = 0, \quad v = 0 \quad \text{at} \quad z = z_0 \tag{7.2.2}$$

The boundary conditions for k and ε are given by Rodi (1993), and couples the bed roughness z_0 to the initial values of k and ε as explained in section 4.4,

$$k = \frac{u_*^2}{\sqrt{C_\mu}} \tag{7.2.3}$$

$$\varepsilon = C_\mu^{3/4} \frac{k^{3/2}}{\kappa z} \tag{7.2.4}$$

At free-surface:

At the free surface zero gradient is applied to all the parameters, hence

$$\frac{\partial u}{\partial z} = 0, \quad \frac{\partial v}{\partial z} = 0, \quad \frac{\partial k}{\partial z} = 0, \quad \frac{\partial \varepsilon}{\partial z} = 0 \tag{7.2.5}$$

8 Field measurements

The field measurements for the tidal current are collected by the University of the Highlands and Islands (UHI), preformed under the MERIKA (Marine Energy Research Innovation and Knowledge Accelerater) initiative. Their goal is to work towards creating a research hub in Europe within the field of renewable marine energy.

The measurements were taken 700 meters outside the coast of the Hebrides during the months of February and May 2013. The mean depth at the location is 12.9 meters. They were conducted with an AWAC (Acoustic Wave and Current) system that uses the Doppler effect to measure the movement of water particles. The sea bed was relatively flat around the position of the measurements, indicating that ocean topology should not effect the recordings. Measurements were done from a distance of 0.75 meters above the sea bed, corresponding to the head of the transducer. From there, recordings of the particle velocities at four locations throughout the water column, hereafter referred to as cell 1, cell 2, cell 3 and cell 4, were made. Their respective distance from the sea bed was 2.15 meters, 4.15 meters, 6.15 meters and 8.15 meters (see figure 8.1).

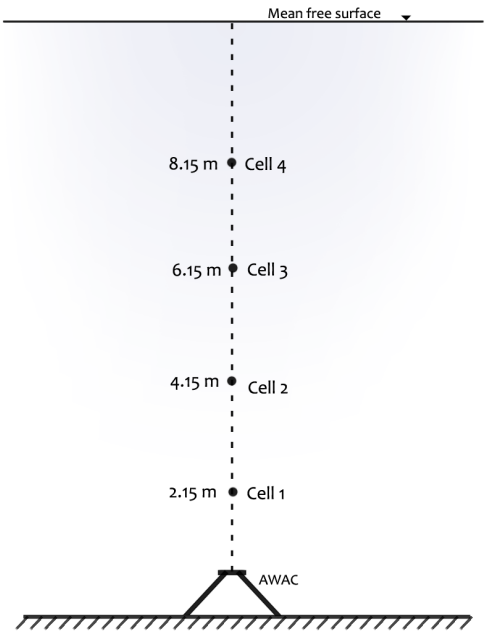

Figure 8.1: Illustration of the AWAC and the vertical position of the measurements relative to the sea bed.

The tidal current velocities was measured every other half an hour with three samplings at 10 minute intervals. Each sampling was done over 10 seconds and the velocities was averaged to get the resulting current velocity. The data was then filtered to remove any frequencies considered to be outside the spectre of the most relevant tidal constituents (see Grønningsæter (2015)).

Figure 8.2 shows the AWAC as positioned on the sea bed. In the background the silhouettes of the aquatic vegetation can be seen.

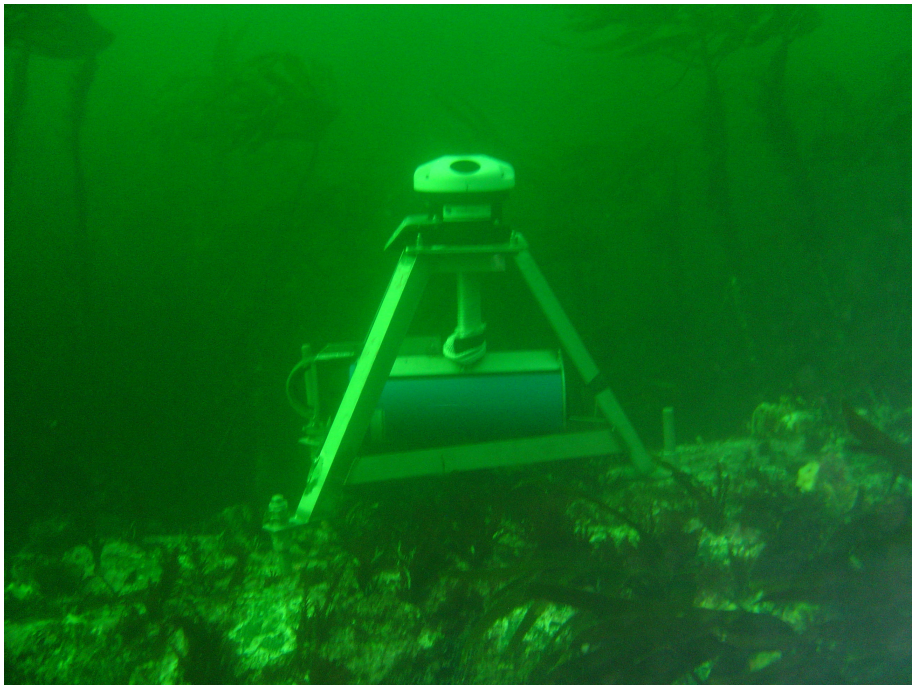

Figure 8.2: Photo showing the AWAC as it sits on the sea bed outside the Hebrids. In the background the silhouettes of the canopy is shown.

Although measurements were taken for both February and May, only the May data will be considered as the February data was effected by a storm occurring in the beginning of that month.

9 Validation against open channal flow through submerged vegetation

Before the k-ε model can be run for tidal flow, the inclusion of the canopy related terms in the governing equations must be validated. All the experiments validated against in this chapter are performed in flumes with steady unidirectional flow. Hence, only the u-component of the velocity is calculated, and the convection terms are still zero. The governing equations are therefore (7.1.4), without the Coriolis term ($f = 0$), and the k-ε equations in (7.1.8) and (7.1.9). Although the flow is steady, the instantaneous velocity term in (7.1.4) is kept for convenience as the code is written for unsteady flows.

Under the boundary layer approximation the pressure gradient is constant (equation (7.1.3)), and is normally defined in the experiments as gravity times an *energy slope* or a *surface slope*, S. Hence, the pressure gradient in equation (7.1.4) is given as

$$-\frac{1}{\rho}\frac{\partial p}{\partial x} = gS, \tag{9.0.1}$$

where $g = 9.81[m/s^2]$ and S is the energy slope defined in the experiments.

The insides of a flume are normally smooth, and the boundary condition at the bottom should theoretically be that of equation (4.4.1) with a smooth roughness parameter, E. However, the turbulence generated from the shear layer at the bottom of the flume will only dominate a thin region closest to the bed before the stem-wake turbulence becomes the dominant source of turbulence (Nepf et al. (1997)). Therefore, the choice of wall function to couple the bed shear stress to the initial values of k and ε will not be of significant importance for the overall results. Hence, the rough boundary condition in equation (7.2.1) is assumed valid if a small bottom roughness z_0 is applied. Nepf et al. (1997) measured the turbulence intensities for emergent vegetation, and found that the bed shear turbulence dominated less than 10 % of the water depth even for sparse stem spacings with a volume fraction ϕ of only 0.6 % (see section 5.1). The remaining boundary conditions are also the same as given in section 7.2.

9.1 Rigid cylinders

For the case of a canopy represented by rigid cylinders, the model has been validated against flume data from Shimizu and Tsujimoto (1994), Dunn et al. (1996) and Ghisalberti and Nepf (2004). The numerical results from the k-ε models of Shimizu and Tsujimoto (1994) and López and García (2001) are also included as part of the validation.

Table 9.1 shows the different parameters needed for the validation. Note that Ghisalberti and Nepf (2004) performed four different trials (B, C, H and J) where they varied several of the parameters given in table 9.1 between each trial.

	$H[m]$	$h[m]$	$a[1/m]$	$S, \times 10^{-5}$	C_D	λ_f
Shimizu and Tsujimoto (1994)	0.0747	0.041	10.0	213	1.0	0.41
López and García (2001)	0.34	0.12	1.09	360	1.13	0.13
Ghisalberti and Nepf (2004) (B)	0.467	0.139	2.5	0.18	1.4	0.35
Ghisalberti and Nepf (2004) (C)	0.467	0.139	3.4	2.5	1.1	0.47
Ghisalberti and Nepf (2004) (H)	0.467	0.138	8.0	10	0.79	1.1
Ghisalberti and Nepf (2004) (J)	0.467	0.138	8.0	1.3	0.92	1.1

Table 9.1: Experimental parameters from the flume experiments presented in López and García (2001), Shimizu and Tsujimoto (1994) and Ghisalberti and Nepf (2004). The parameters H, h, a, S, C_D and λ_f are the water depth, canopy height, frontal area per volume (5.1.1), energy slope, drag coefficient and roughness density (5.1.2), respectively.

The experimental parameters presented in López and García (2001) are the ones used by Dunn et al. (1996) in their experiments. Unidirectional flow was run through a recirculating flume. The canopy was represented by rigid vertical cylinders mounted onto a false bottom plate. Their arrangement was in a staggered pattern with variable density. A honeycomb grid was positioned upstream of the canopy in order to straighten the inflow onto the canopy. Velocity profiles were measured at four different locations in the longitudinal direction of the tank. Each profile consisted of 10 measurement points each. These profiles were then spatially averaged to obtain the resulting mean velocity profile for the canopy. All the velocity profiles were measured inside the stem wakes, however it was stated that they were not measured too close. The measuring locations were also taken far enough downstream of the leading edge of the canopy in order to avoid transitional effects.

Although Dunn et al. (1996) measured changing values for the canopy drag coefficient, the mean value of $C_D = 1.13$ is used for the present model in accordance with López and García (2001). The modelled velocity profile, using the same input parameters as the numerical model of López and García (2001) in table 9.1, has been plotted against the predicted velocity profile from their k-ε model and the experimental data from Dunn et al. (1996). The comparison is displayed in figure 9.1.

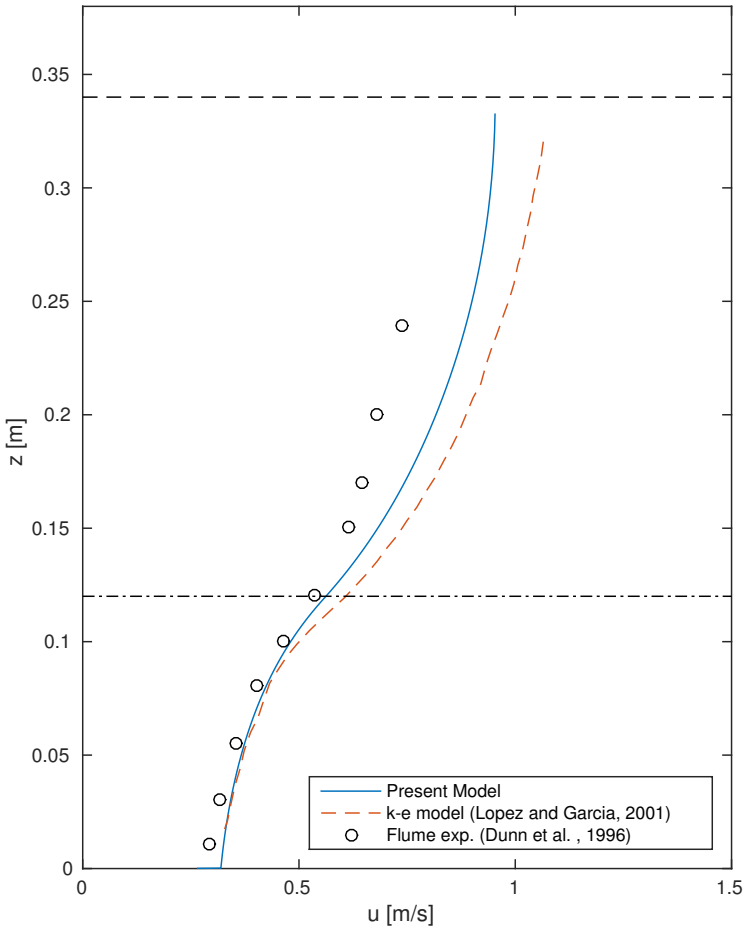

Figure 9.1: Comparison of the predicted velocity profile between the present k-ε model, the k-ε model from López and García (2001) and experimental data from Dunn et al. (1996). u is the spatially averaged mean velocity and z is the water depth. The vertical dashed and dash-dot line indicate the water surface H and the canopy height h, respectively.

It can be noticed from figure 9.1 that the boundary layer closest to the wall becomes extremely thin. Therefore, the characteristics of the no-slip boundary condition in equation (7.2.2) is not obvious. However, this is connected with the bottom roughness z_0 being small, and that the model is not able to resolve such a thin layer close to the wall. However, the no-slip boundary condition is incorporated and the effect of the bottom roughness is insignificant for the reasons mentioned in the beginning of this chapter. The same applies for the rest of the modelled velocity profiles in this chapter.

To further justify the use of a bottom roughness for the prediction of flume data, appendix B shows the resulting velocity profiles from running the model with different values for z_0. They are compared against the flume data from Dunn et al. (1996) and the rest of the input parameters are the ones given by López and García (2001) in table 9.1.

Besides from that, it can be seen that our model predicts the experimental velocity profile in figure 9.1 well. Both k-ε models coincide well with the experimental results within the canopy height. Above the canopy both the present model and the model of López and García (2001) overpredicts the results. However, the present model predicts the above-canopy flow with better accuracy than the one from López and García (2001).

The reason behind these different results produced by two apparently equal k-ε models may come from the calculation López and García (2001) uses to find the eddy viscosity ν_t in (4.3.1). Instead of applying the generally accepted coefficient $C_\mu = 0.09$, they used an iterative calculation process (see López and García (2001)), hence introducing C_μ as a depth dependent variable. They also used a Dirichlet boundary condition for the dissipation at the surface as opposed to the Neumann condition in (7.2.5).

Shimizu and Tsujimoto (1994) compared their numerical results with flume measurements over a canopy of equally spaced rigid cylinders. The velocity profiles were found using a hot-film anemometer. Figure 9.2 shows the modelled velocity profile from the present model, plotted against the numerical and experimental results presented by Shimizu and Tsujimoto (1994).

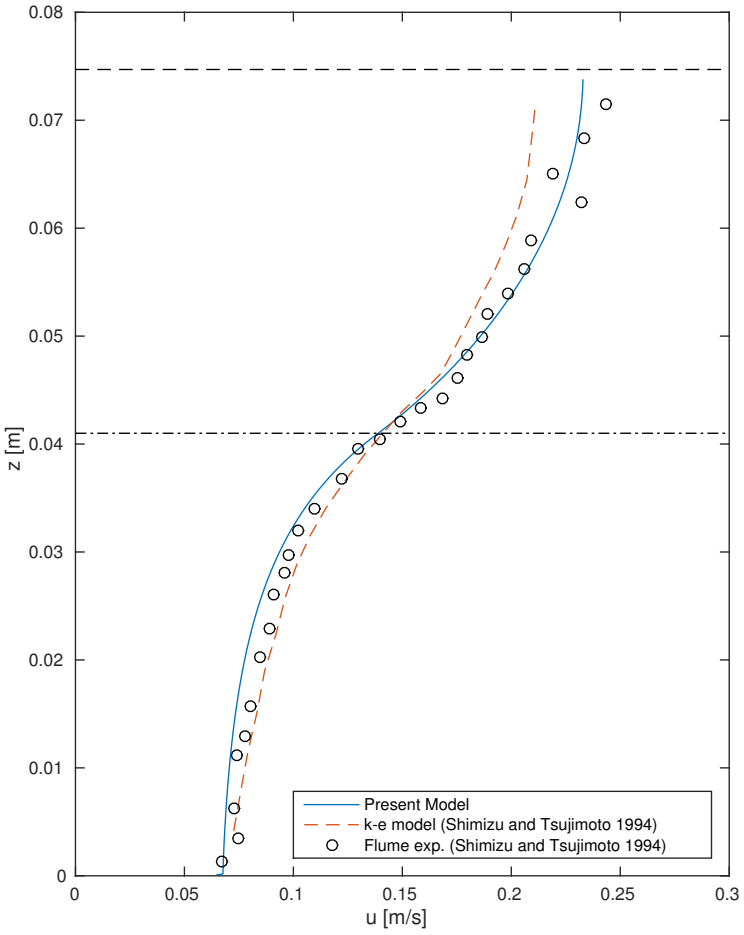

Figure 9.2: Comparison of the predicted velocity profile between the present k-ε model, the k-ε model from Shimizu and Tsujimoto (1994) and flume experiments presented by Shimizu and Tsujimoto (1994). u is the spatially averaged mean velocity and z is the water depth. The vertical dashed and dash-dot line indicate the water surface H and canopy height h, respectively.

The comparison in figure 9.2 is promising, and the present model predicts the flume experiments accurately throughout the whole water column.

The results also shows a good fit with the numerical results from Shimizu and Tsujimoto (1994). However, they used different values for the coefficients C_{fk} and $C_{f\varepsilon}$ than the ones adopted from López and García (2001) for the present model. Instead of the more theoretical values of $C_{fk} = 1$ and $C_{f\varepsilon} = 1.33$, they determined the coefficients from numerical fitting with flume data (not with the presented data in figure 9.2). From doing so they ended up with $C_{fk} = 0.07$ and $C_{fe} = 0.16$. That is a significant difference from López and García (2001). Based on the reasoning in section 6.2 and 6.3 this corresponds to only 7 % of the work done by the mean flow against the stems is being transformed into wake-turbulence. However, the low coefficient for the wake-generated turbulence

is coupled with a corresponding low coefficient for the wake dissipation, although the proposed relation in equation (6.3.4) does not hold.

Based on the reasoning in section 6.2 and 6.3, and the results of figure 9.2, the coefficients from López and García (2001) are considered more suited for the present model.

Contrary to Dunn et al. (1996), Ghisalberti and Nepf (2004) averaged their experimental results in the crosswise direction of the tank. They used three 3D acoustic Doppler velocimetry (ADV), and pointed out the importance of the recordings being done outside of the sidewall boundary layers. The cylinders were spaced randomly, and the inflow was first run through a vertical grid of cylinders to remove inherent turbulence and then straightened. The experimental flume data, along with the predicted velocity profile from the present k-ε model, are displayed in figure 9.3.

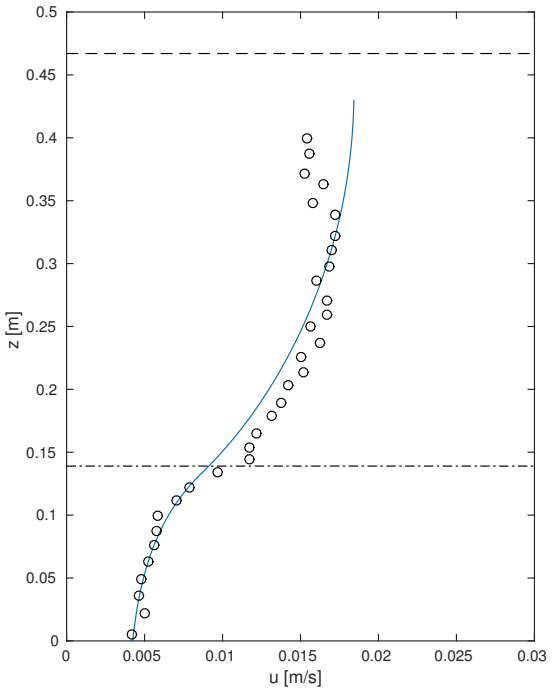

(a) Exp. B ($\lambda_f = 0.35$)

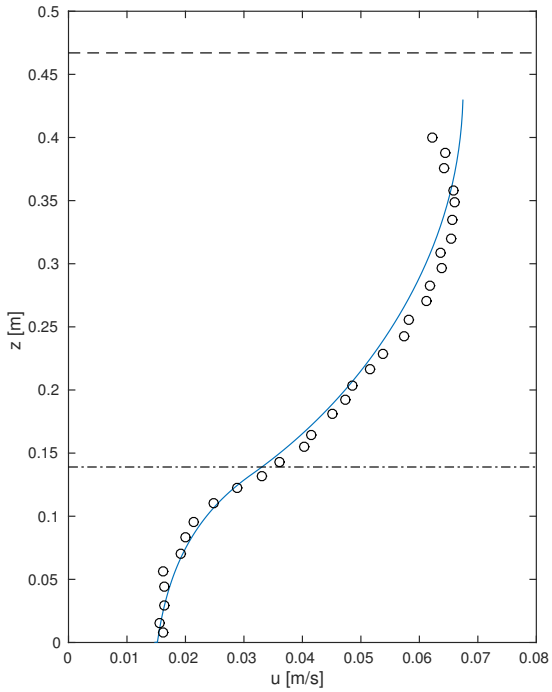

(b) Exp. C ($\lambda_f = 0.47$)

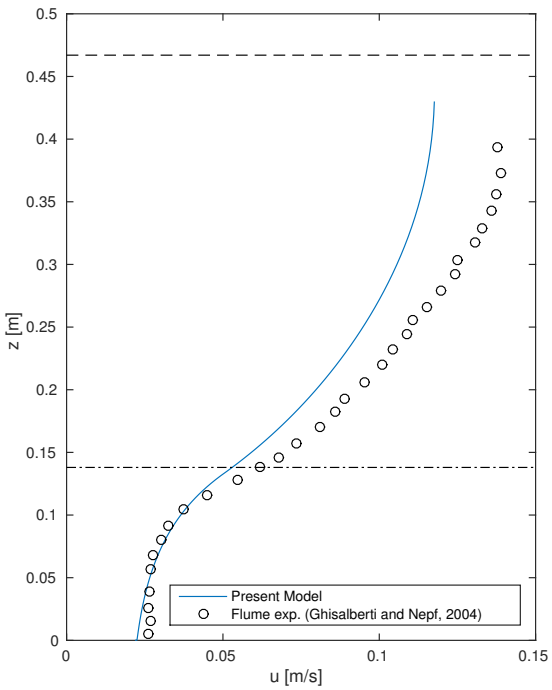

(c) Exp. H ($\lambda_f = 1.1$)

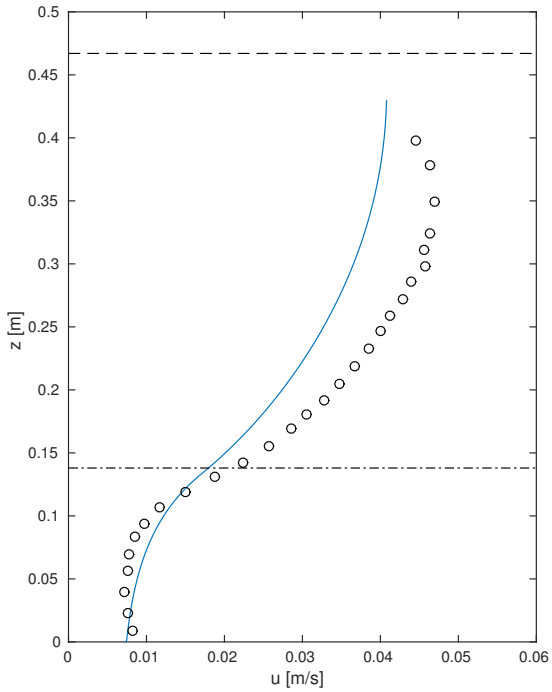

(d) Exp. J ($\lambda_f = 1.1$)

Figure 9.3: Comparison of the predicted velocity profile from the present model and flume experiments performed by Ghisalberti and Nepf (2004). u is the spatially averaged mean velocity and z is the water depth. The vertical dashed and dash-dot line indicate the water surface H and canopy height h, respectively.

It is seen that the model predicts the mean velocity profile for experiment B (figure 9.3a) and C (figure 9.3b) particularly well, with a close fit over the whole water depth. Against experiment H (figure 9.3c) and J (figure 9.3d) the model accurately predicts the mean velocity within the canopy. However, above the canopy the mean velocity is underpredicted by the model for both experiment H and J. This is opposite of the overpredicion encountered for the data from Dunn et al. (1996) in figure 9.1. The results from figure 9.3 are interesting as erroneous effects due to the measuring equipment and flume set-up does not effect the relative trend between the predicted profiles and the data. Hence, the trend of underpredicted velocity above the canopy, for high canopy densities, stands stronger than the trend of overprediction for relative sparse canopies from the one experiment by Dunn et al. (1996).

The modification of the dissipation due to canopy-scale vortices given by Uittenbogaard (2003) (see section 6.4) was implemented for experiment H and J. Ghisalberti and Nepf (2004) estimated these runs to have slightly larger canopy-scale vortices than experiment B and C. However, the modification gave no alteration of the results. The general observation during this study has been that increasing the production of ε contributes only in removing energy from the system, hence reducing the mean velocity even more. However, no thorough investigation of this tendency was performed.

Based on the observations in figure 9.1 - 9.3, a very coarse statement can be made that our model works best within the range of $0.13 < \lambda_f < 1.1$. When $\lambda_f = 0.13$ the model overpredicts the mean velocity above the canopy, while for $\lambda_f = 1.1$ the mean velocity appears to be underpredicted for the same region. Within the canopy all the modelled velocity profiles accurately predicts the flume data. Naturally, investigation of a wider spread of densities has to be performed to firmly make such a statement.

It should also be pointed out that there are other flow parameters being changed between the runs than just the roughness density. Comparison between the densities are chosen as its importance on the generation of canopy-scale vortices are emphasized by Nepf (2012a) (chapter 5).

Nepf (2012a) states that canopy-scale vortices occurring for canopies with $\lambda_f \approx 0.1$ will penetrate all the way to the sea bed. This will alter the turbulent transport throughout the whole canopy layer, as well as the turbulent transport from the canopy to the above-canopy flow. This might explain some of the discrepancy between the modelled velocity above the canopy and the flume data from Dunn et al. (1996). However, it does not explain the good prediction of the mean velocity within the canopy.

It should also be pointed out that Ghisalberti and Nepf (2004) obtained significantly better velocity predictions for experiment H, using their own numerical code. Their model is based entirely on the conservation of shear-generated, canopy-scale, turbulence between the canopy and the unobstructed flow, and its dissipation to stem-scaled turbulence as the vortices penetrate the canopy. However, the underlying assumptions behind their model is not directly compatible with the present k-ε model.

9.2 Flexible vegetation

A thorough investigation of flow through a flexible canopy was performed by Nepf and Vivoni (2000). The flume used is the same as in Ghisalberti and Nepf (2004). The flexible plants consisted of six thin vinyl blades attached to a short stem. The geometry and rigidity are made to simulate that of real vegetation. Velocity measurements were performed using both acoustic Doppler velocimetry and laser Doppler velocimetry, and were measured far enough downstream to avoid the transitional effects from the canopy's leading edge. Three measurements were taken in the lateral direction and then spatially averaged.

The frontal area per volume, a, is varying with the plant height. Nepf and Vivoni (2000) estimated a by tracing the shape of 10 individual plants over grid paper and then averaging the results. The drag coefficient is also depth dependent, and was calculated from the steady momentum equation using the Reynolds stress as measured in the experiment. Both the depth varying frontal area per volume $a(z)$ and the depth varying drag coefficient $C_D(z)$ was incorporated into the present model. Table 9.2 shows the relevant parameters.

	$H[m]$	$h[m]$	$a[1/m]$	$S, \times 10^{-4}$	C_D	λ_f
Nepf and Vivoni (2000)	0.44	0.16	$a(z)$	2.0	$C_D(z)$	0.71

Table 9.2: Flume data from Nepf and Vivoni (2000) for submerged flexible vegetation. The parameters H, h, a, S, C_D and λ_f are the water depth, canopy height, frontal area per volume (5.1.1), energy slope, drag coefficient and roughness density (5.1.2), respectively. a and C_D are depth dependent (see Figure 3 in Nepf and Vivoni (2000))

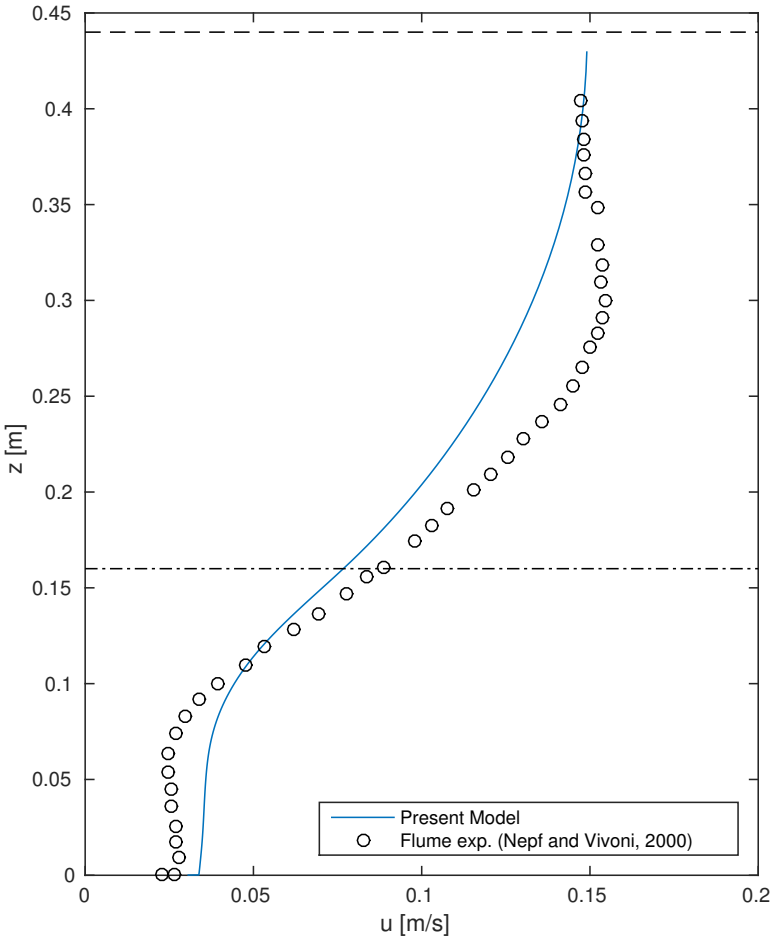

Figure 9.4: Comparison of the predicted velocity profile from the present model and flume experiments performed by Nepf and Vivoni (2000). u is the spatially averaged mean velocity and z is the water depth. The vertical dashed and dash-dot line indicate the water surface H and canopy height h, respectively.

Figure 9.4 shows the comparison between the present model and the experimental results by Nepf and Vivoni (2000). The velocity profile appears to be overpredicted within the canopy and underpredicted above the canopy. Following the analogy of having a particular density interval for which the model is valid, this indicates that the upper limit of $\lambda_f = 1.1$ should be lowered to $\lambda_f = 0.71$. However, in contrast to figure 9.3c and 9.3d, the mean velocity within the canopy is not equally well predicted.

Regarding the applicability of inserting $a(z)$ and $C_D(z)$ directly into the model, it is uncertain if $a(z)$ were obtained for plants at rest or under the impact of the current. This would probably be of some importance as C_D was measured from a state where the plants were under impact of the current.

Dijkstra and Uittenbogaard (2010) compared their numerical model with the same ex-

perimental data as in figure 9.4, but used a different pressure gradient to drive the flow. Instead of using the surface slope S as given in the experiment, they tuned S until it gave the same depth averaged velocity as the experimental results. Compared to the modelled velocity profile in figure 9.4 this corresponds to an increase of the pressure gradient (gS). Applying the same procedure for our model we get the results in figure 9.5. The boundary conditions was lowered slightly to correspond to the range of given experimental points.

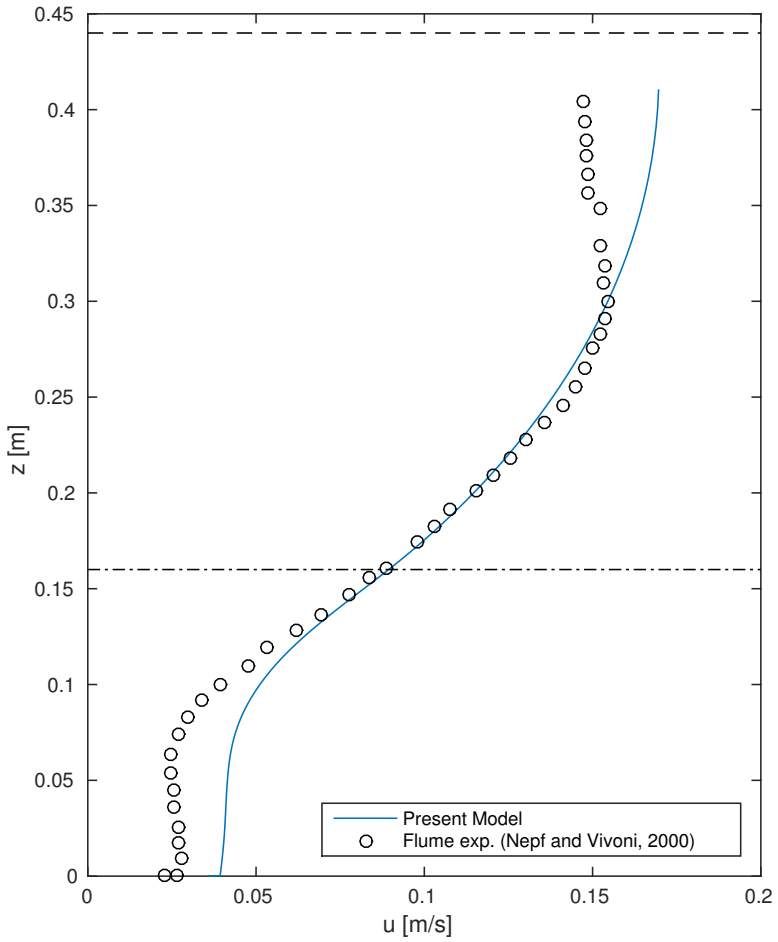

Figure 9.5: Comparison of the predicted velocity profile from the present model and flume experiments performed by Nepf and Vivoni (2000), when driving the flow with pressure gradient corresponding to a depth averaged velocity of $0.10\,m/s$. u is the spatially averaged mean velocity and z is the water depth. The vertical dashed and dash-dot line indicate the water surface H and canopy height h, respectively.

There is a general improvement in the middle depth range, of the mean velocity prediction between figure 9.4 and 9.5. Because the pressure gradient is constant, increasing it naturally results in a more overpredicted mean velocity within the canopy, while the underpredicted velocity above the canopy is improved.

The flume data given in figure 9.3a–9.5 shows a backward facing mean velocity in the vicinity of the free surface. Because the same flume has been used to obtain all this data, this tendency is assumed to be due to be erroneous effects related to the flume, and not actual physical results.

Dijkstra and Uittenbogaard (2010) incorporated the flexibility of the plants into their k-ε model. However, they state that this was not a governing factor for the results as the plants used by Nepf and Vivoni (2000) was relatively rigid. They also used the modification for the wake dissipation by Uittenbogaard (2003) (see section 6.4). This was also implemented into the present model. However, the implementations did not effect the results.

In summary, it appears that the canopy-related implementations performed for the present model is able to reproduce the boundary layers of unidirectional flow thorough submerged vegetation with acceptable accuracy. Especially the velocities within the canopy is well predicted by the present model.

10 Wave-current interaction on flow through submerged vegetation

In many real life applications waves will occur alongside currents. To investigate the applicability of the model with regards to wave-current interactions, it was run against experimental flume data performed by Hu et al. (2014). They used stiff wooden rods to represent the submerged vegetation, and had them uniformly spaced along a false bottom inside the flume. The velocity was measured by four EMFs (Electromagnetic Flow Meters) probes within the canopy, spaced one meter apart in the longitudinal direction. The velocity profiles at each EMF were obtained by moving the EMFs vertically. Then spatial averaging of the individual profiles were performed to obtain a representative mean velocity profile for the canopy. In addition to wave-current measurements, Hu et al. (2014) performed comparison trials for the cases of pure current and pure waves through the same canopy.

Forces acting on four individual stems, also spaced one meter apart in the downstream direction, were measured by directly attaching the cylinders to force transducers mounted into the false bottom. Through spatial averaging, the drag coefficient for the canopy was estimated with respect to changing Reynolds number, Re. For pure wave and wave-current flow Hu et al. (2014) obtained the following analytical expression for the drag coefficient as function of Re,

$$C_D = 1.04 + \left(\frac{730}{Re}\right)^{1.37} \qquad 300 < Re < 4700. \tag{10.0.1}$$

Here, the Reynolds number is defined as

$$Re = \frac{U_{max} d}{\nu}, \tag{10.0.2}$$

where d is the stem diameter ($d = 0.01$m), ν is the kinematic viscosity, and U_{max} is given as $U_{max} = U_{mean} + U_w$. U_w is the amplitude of the horizontal component of the particle velocity at the free surface, and U_{mean} is to be understood as the depth averaged current velocity acting on the canopy when accounting for the effect of the wave-current damping (see section 4.5).

The measured drag force is not given for the relevant velocity profiles. For consistency the formulation in equation (10.0.1) will be used to find the drag coefficient going into the canopy drag force in equation (7.1.6). Only the depth averaged velocity for a pure current through the canopy is given explicitly in the paper ($U_c = 0.15\, m/s$). Hence, U_{mean} has to be estimated. Using the resulting velocity profile for the wave-current flow given in Hu et al. (2014), U_{mean} was estimated as $U_{mean} = 0.13\, m/s$. Because their velocity measurements does not cover a significant portion of the water column closest to the surface, this will be a crude estimate.

Under this assumption the resulting drag coefficient for wave-current flow is calculated using (10.0.1) and (10.0.2). With $U_w = 0.20\,m/s$, the result is as displayed in table 10.1.

	$U_{max}[m/s]$	Re	C_D
wave-current	$U_{max} = U_{mean} + U_w = 0.33$	3300	1.17

Table 10.1: Reference velocity U_{max} for wave-current flow with resulting Reynolds number Re and drag coefficient C_D.

Equation (10.0.1) is not confirmed to hold for pure current flow. It is assume that the drag coefficient for the current is approximately the same as for the wave-current flow.

In addition to the pressure induced by the waves, the wave-current flow will have a pressure component due to the current as well. Assuming these can be superpositioned the following pressure gradient goes into equation (7.1.4),

$$-\frac{1}{\rho}\frac{\partial P}{\partial x} = -\zeta_A \omega^2 sin(\omega t) + gS. \tag{10.0.3}$$

The first term on the right hand side of (10.0.3) is the hydrostatic pressure gradient due to the waves, where ζ_A is the wave amplitude, $\omega = 2\pi/T$, and T is the wave period. The last term is the constant pressure gradient due to the current alone. The terminology from equation (9.0.1) is kept, although referring to a *surface slope* S is inappropriate when the surface is covered with waves.

As noted, the boundary layer approximation is assumed valid for the wave-current flow. Hence the dynamic pressure from the waves is assumed to be constant throughout the water depth in accordance with equation (7.1.3). This is not completely accurate as the vertical particle velocity at the top of the surface is of the same order as the horizontal velocity. However, the assumption becomes more accurate towards the bottom of the flume as the vertical particle velocity decreases exponentially with the depth.

Because no pressure gradient is given as input by Hu et al. (2014), the pressure gradient due to the current (in practice meaning S) was tuned until the total pressure gradient for the wave-current flow generated a depth averaged velocity corresponding to $U_{mean} = 0.13\,m/s$. The same procedure was followed for the pure current flow, only with $U_c = 0.15\,m/s$, instead of U_{mean}.

The relevant flume parameters, along with the estimated depth-averaged velocity for the wave-current flow, are given in table 10.2.

	$H[m]$	$h[m]$	$a[1/m]$	$C_D[-]$	$\zeta_A[m]$	T [s]	$\overline{U}[m/s]$	λ_f
pure current	0.5	0.36	5.55	1.17	-	-	0.15	2.0
pure waves	0.5	0.36	5.55	1.30	0.05	1.6	-	2.0
wave-current	0.5	0.36	5.55	1.17	0.05	1.6	0.13	2.0

Table 10.2: Flume data from Hu et al. (2014). The parameters H, h, a, C_D, ζ_A, T, $\overline{U}$ and λ_f represents the water depth, canopy height, frontal area per volume, drag coefficient, wave amplitude, wave period, depth averaged velocity and roughness density, respectively.

The model can not be run for the case of pure waves as the boundary layer approximation does not hold. However, the experimental results from Hu et al. (2014) are shown in figure 10.1 as they illustrate a negative period averaged velocity profile for the case of only waves. It should be mentioned that this backward going current also occurred in the experiment when waves were run through the flume without the canopy present. This indicates that the entire discrepancy can not be coupled to the waves interacting with the canopy, but rather more inherent effects. If the waves in the experiment were not perfectly sinusoidal this could lead to a resulting current when averaging over the intentional wave period. This could be a result of friction between the waves and the side walls in the case of no vegetation, but could also be coupled to the vegetation when this was present. Figure 10.1 therefore indicates that there may be a similar effect on the wave-current data.

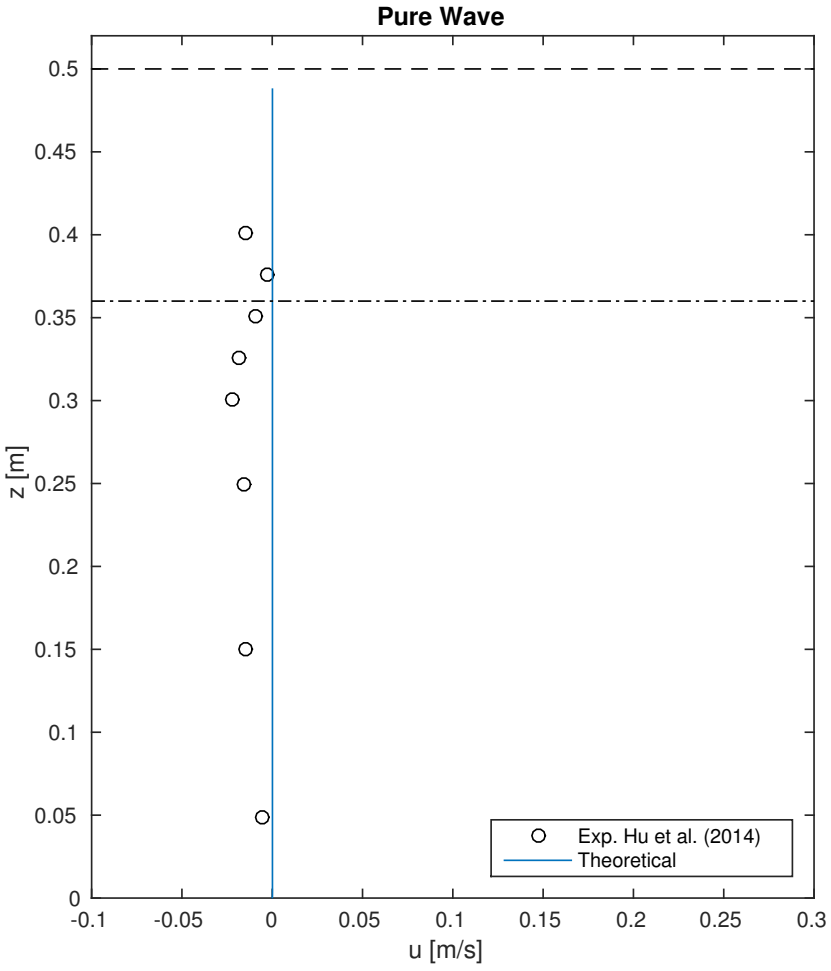

Figure 10.1: Experimental data from Hu et al. (2014) for waves propagating through a submerged canopy. Plotted against the theoretical period averaged velocity if second order effects are neglected. u is the period averaged velocity and z is the water depth. The vertical dashed and dash-dot line indicate the water surface H and the canopy height h, respectively.

Before running the model for wave-current flow, it was compared against the pure current flow similar to the validation in chapter 9. Figure 10.2 shows the modelled velocity profile plotted against the experimental result from the case of a pure current through the submerged canopy. Interestingly, the results somewhat contradicts the findings in chapter 9 where the model was found to underpredict the above-canopy velocity when the density became large ($\lambda_f = 1.1$). However, the H/h-ratio is significantly smaller in this experiment than what was used by Ghisalberti and Nepf (2004) in figure 9.3c and 9.3d. For $H/h < 2$, the constraints on the canopy-scale vortex growth due to the surface is believed to be significant (Nepf and Vivoni (2000)). With a ratio of $H/h \approx 1.4$, the experiments from Hu et al. (2014) are well within this region. This indicates that the canopy-scale vortices predicted to occur in the experiments from Ghisalberti and Nepf (2004) will be confined by the free surface in the experiments of Hu et al. (2014). Hence,

they will have limited growth possibilities and a smaller chance of affecting the flow. This might be the reason why the model manage to more accurately predict the data from Hu et al. (2014) than the data from Ghisalberti and Nepf (2004) for such high canopy densities.

In accordance with chapter 9, the mean velocity within the canopy in figure 10.2 is well predicted by the present model.

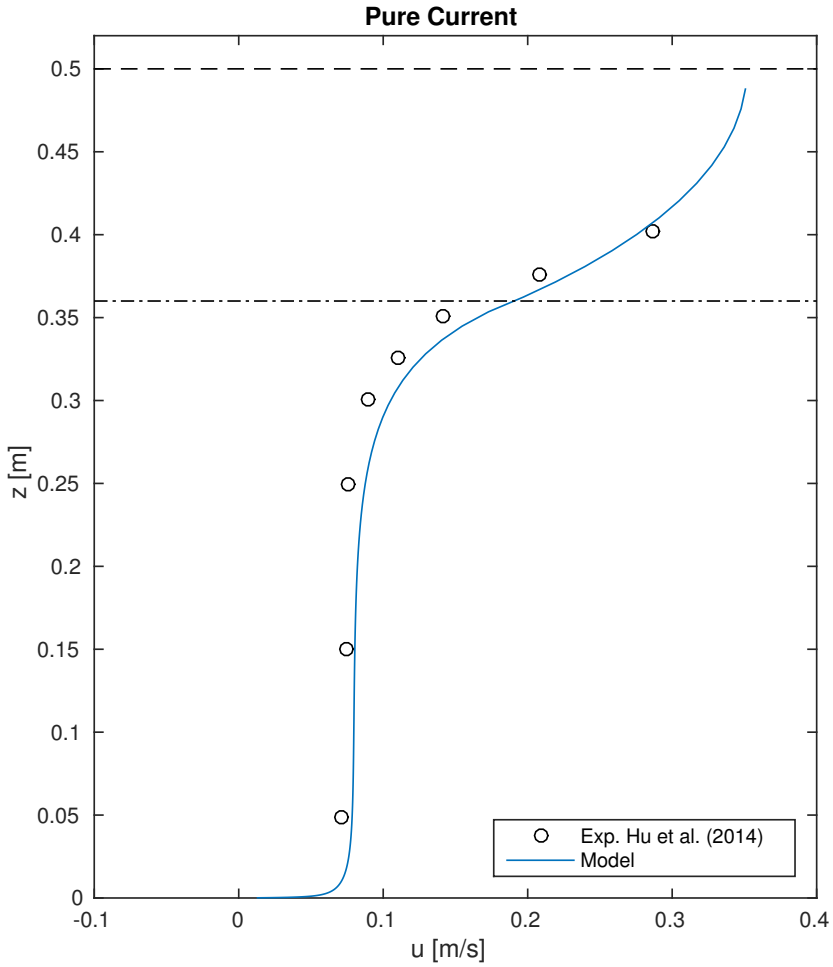

Figure 10.2: Predicted mean velocity profile plotted against experimental measurements from Hu et al. (2014) for a current through a submerged canopy. u is the spatially averaged mean velocity and z is the water depth. The vertical dashed and dash-dot line indicate the water surface H and the canopy height h, respectively.

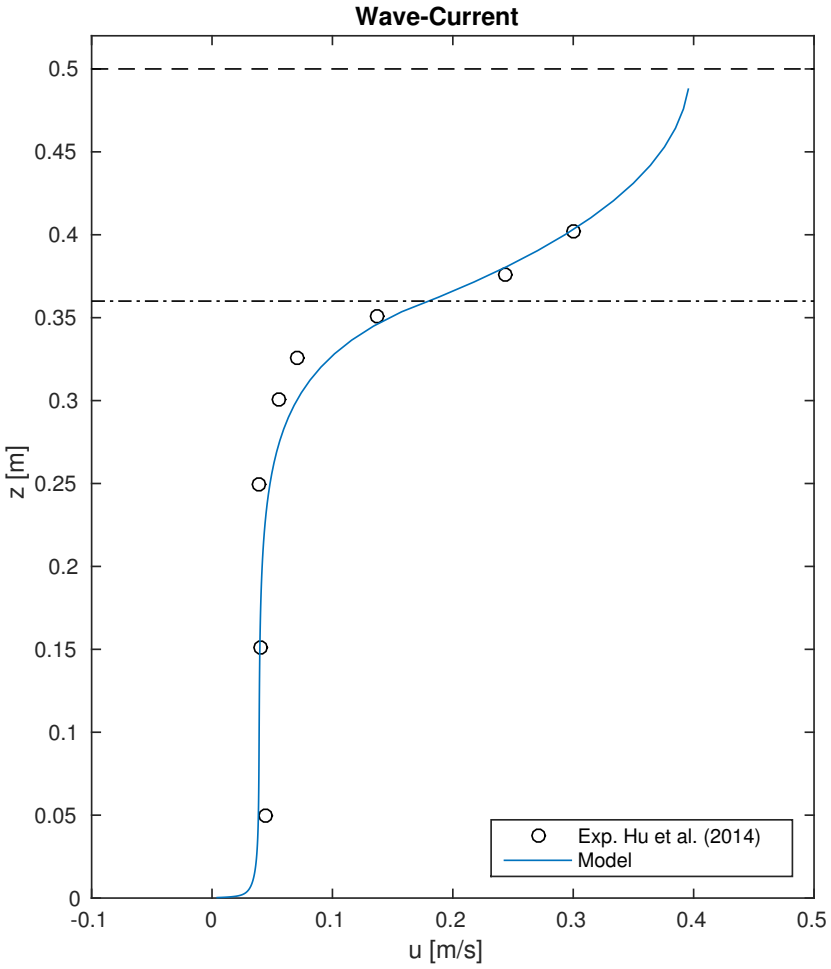

Figure 10.3: Predicted mean velocity profile plotted against experimental measurements from Hu et al. (2014) for both current and waves moving in the same direction through a submerged canopy. u is the unidirectional spatially averaged mean velocity and z is the water depth. The vertical dashed and dash-dot line indicate the water surface H and the canopy height h, respectively.

By implementing the pressure gradient in equation (10.0.3), the wave-current flow was predicted. Figure 10.3 shows the modelled velocity profile for the wave-current flow plotted against the experimental data from Hu et al. (2014). The comparison shows that the model manage to accurately reproduce the velocity profile from the experiments. However, the effects causing the negative current for pure waves in figure 10.1 will most probably also be present in the case of wave-current flow. If these effects causes a positive or a negative current is difficult to predict as the reactions causing these effects may change from the state of pure current to the state of wave-current flow. The same goes for its magnitude. However, it is fair to mention this possible discrepancy when validating the applicability of the model for the case of wave-current flow.

It should also be mentioned that the *energy slope* S needed to drive the wave-current flow had to be twice of that used to drive the pure current flow. Only then did the model produce the depth averaged velocity of $U_{mean} = 0.13m/s$.

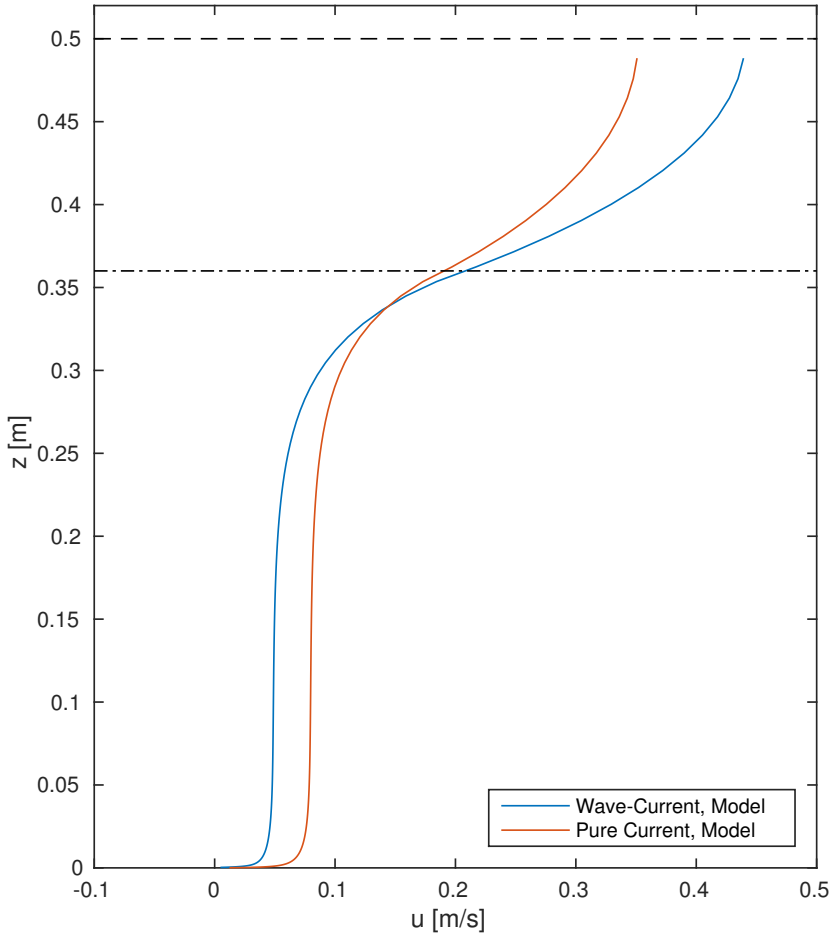

Figure 10.4: Comparison between the numerically predicted velocity profiles for the case of pure current and wave-current flow through a submerged canopy. u is the spatially averaged mean velocity and z is the water depth. The vertical dashed and dash-dot line indicate the water surface H and the canopy height h, respectively.

A comparison between the velocity profile from the pure current and wave-current flow is plotted in figure 10.4. Although the damping due to the wave-current interaction is inherent due to the way the pressure gradient was set, it is consistent with the findings of Hu et al. (2014) within the range of their measurements.

The case of wave-current flow over submerged vegetation is an interesting topic. The particle trajectories that are damping the flow in the case of unobstructed wave-current flow does not automatically give the same effect when vegetation is covering a significant

part of the water column.

However, as only one validation against wave-current data were performed in this study, further validation is needed to conclude the applicability of the wave-current implementation. Especially the high pressure gradient needed to obtain the correct depth average velocity is of concern. If the pressure gradient due to the current is fixed, it's doubtful that it will be able to overcome the heavy damping of the mean velocity resulting from the wave-current implementation. Therefore, the effect of wave-current flow is not implemented when modelling the tidal boundary layers.

11 Tidal flow through submerged vegetation

The model in chapter 7 will be run against the tidal measurements from the Hebrides (see chapter 8). As opposed to the unidirectional current and wave-current flows in chapter 9 and 10, the constant pressure gradient will now be determined from the velocity time series using equation (7.1.14) and (7.1.15). Wave-current effects are not included for the following simulations.

11.1 Plant properties

The largest uncertainty for the following calculations is that of determining a reasonable frontal area per volume, a, and drag coefficient, C_D, to represent the canopy at the location of the measurements. These two parameters are crucial for the representation of the drag force induced on the flow by the vegetation. The plant species is of the type *Laminaria hyperborea*. This specie is characterized by a long circular stem with a dense bundle of leafs at the top. The contour of the plants can be seen in the background of figure 8.2. The stem is quite robust and stiff, justifying that it can be modeled as a rigid circular cylinder. However, from figure 8.2 the leafs appear to be more flexible, and are bending under the impact of the current. Because the model does not account for plant flexibility, the leafs must be simplified in a manner that accounts for their damping of the flow. As a simple estimate, the leafs are modelled as ellipses cut along their minor axis. The relative size of the minor and major axis must be determined from what gives the the best representation of the drag, rather than the shape itself. This is because the model treats any surfaces as a rigid solid object, meaning that the shape of the leaf must be smaller than what their contours indicate in order to avoid overpredicting the drag.

Figure 11.1 shows the estimated leaf shape, along with its variable semi-minor (ax) and semi-major (by) axis.

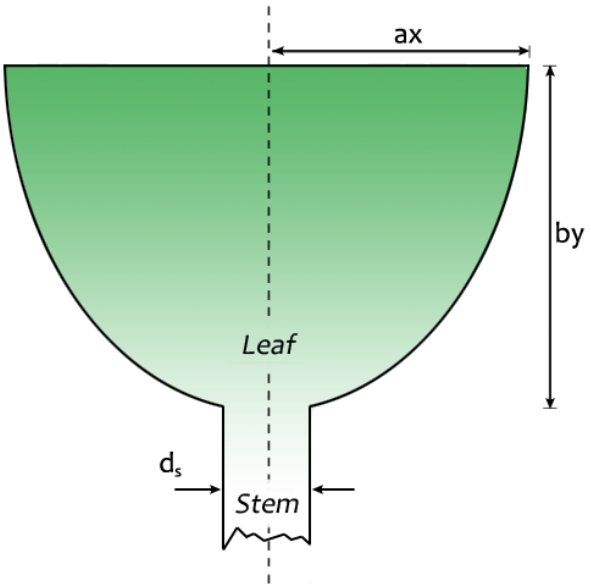

Figure 11.1: Illustration showing the leaf shape estimated as an ellipse cut along its minor axis. Hence, ax and by is the semi-minor and semi-major axis, respectively. d_s is the stem diameter.

11.2 Parameter comparison

Because the relative size of the plant parameters discussed in the section above are unknown, the model will be run against several plant properties to investigate how each effects the result. Assuming an equally spaced grid of plants, the frontal area per volume, a, can be found by the plant diameter d and the stem spacing ΔS. The stem diameter will be constant and are denoted d_s. However, the overall plant diameter d will be depth dependent due to the leaf geometry given by ax and by. Hence, the frontal area per volume (see equation (5.1.1)) will be depth dependent.

A total of seven different runs are preformed. Table 11.1 gives a description of each model along with their input parameters.

Model	H[m]	$h[m]$	$d_s[m]$	$\Delta S[m]$	C_D	$ax[m]$	$by[m]$	λ_f
A1	12.9	3	0.08	3	1	0.3	0.5	0.048
A2	12.9	3	0.08	3	1	0.2	0.4	0.037
A3	12.9	3	0.08	3	1	0.1	0.3	0.029
A2S4	12.9	3	0.08	4	1	0.2	0.4	0.021
A2S5	12.9	3	0.08	5	1	0.2	0.4	0.013
A2H2	12.9	2	0.08	3	1	0.2	0.4	0.028
A2H4	12.9	4	0.08	3	1	0.2	0.4	0.046

Table 11.1: List of the different input parameters used for running the model. H is the mean water depth,h the canopy height, d_s the stem diameter, ΔS the stem spacing, C_D the plant drag coefficient, λ_f the roughness density, and ax and by the semi-minor and semi-major axis of the leaf area, respectively.

As stated, the stem diameter d_s is kept constant. Taking into account the growth of algae on the plant stems, as seen from figure 8.2, an estimated diameter of $d_s = 8\,cm$ seems to be a reasonable approximation. Because ΔS is significantly larger than d_s, changing d_s will have a minimal effect on the frontal area per volume, a.

Figure 11.2 shows the relative decrease in leaf area between the three runs A1, A2 and A3. In the following calculations it is assumed that the frontal area of the leaf is positioned perpendicular to the flow. Because the flow is two dimensional in the horizontal plane, the frontal area per volume, a, of the leaf is decomposed into a x- and y-component. The stem is circular, hence no decomposition of a is needed over the stem.

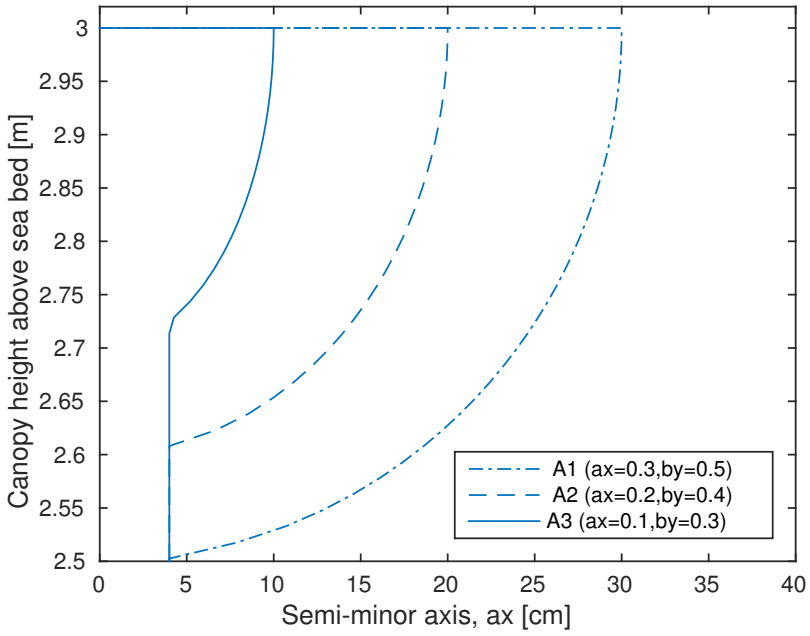

Figure 11.2: Plot showing the three different leaf areas used in the model runs A1, A2 and A3.

It should also be noted from table 11.1 that the drag coefficient is assumed to be constant over the whole canopy height. Because the shape of the plant starts as a cylinder at the stem and transforms into more of a plate at the leaf this is most certainly not the case. However, the effect of an increasing form drag at the leaf will be somewhat similar to an increase of the leaf area itself. Therefore, the drag coefficient will be kept constant for the sake of simplicity.

In figure 11.3 the modelled mean velocities for the different leaf areas have been plotted against the field data taken during May (see chapter 8). For comparison, the result from running the model using only the bed roughness z_0 is included. The bed roughness used is $z_0 = 0.0006\,cm$ which was found to give the best fit with the May data when not accounting for the vegetation (see Grønningsæter (2015)). The velocity profile from using only the bed roughness is reproduced under the same procedure as in Grønningsæter (2015). The reason why the present model covers more of the water depth is because it was run with 200 grid points as opposed to 100. This was done to increase the number of computational nodes over the leaf area.

Regardless of the different leaf areas, figure 11.3 shows that the velocity prediction of the lower three measurement points of the May data is greatly improved by accounting for the vegetation. However, the top data point is more accurately predicted by only using a bed roughness. Besides that, it is also noted that the relative small differences in leaf area between A1, A2 and A3 has a significant impact on the in-canopy velocity. This is the case despite of the vertical extend of the leaf area only being a fraction of the vertical extend of the stem.

Above the canopy, the mean velocity profiles for both A1, A2 and A3 appear to converge towards a fixed value. This is reasonable as the effect of the wake-scaled turbulence should diminish with increasing distance from the canopy. However, the result using only the bed roughness z_0, converge to a different mean velocity towards the free surface than the results from A1, A2 and A3. This indicates that the numerical effect of including the canopy does not diminish entirely towards the free surface.

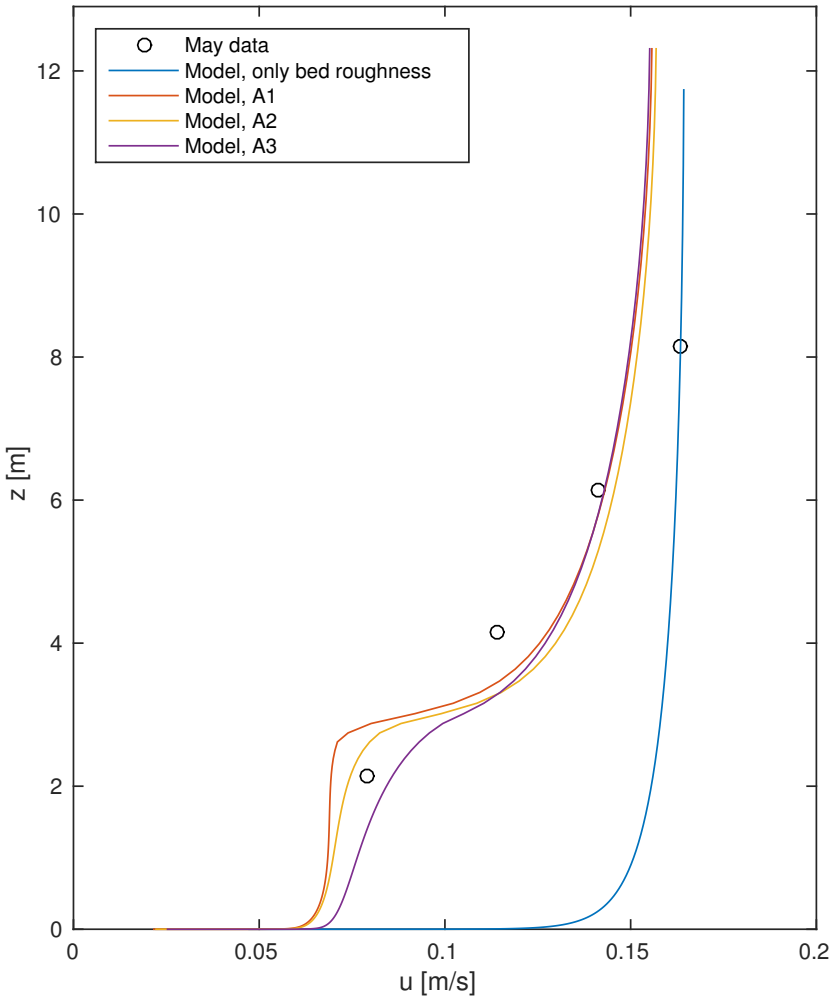

Figure 11.3: Comparison between the modelled velocity profile using different leaf areas, the field data from May, and the modelled velocity using only the bed roughness ($z_0 = 0.0006\,cm$). u is the spatially averaged mean velocity and z is the water depth.

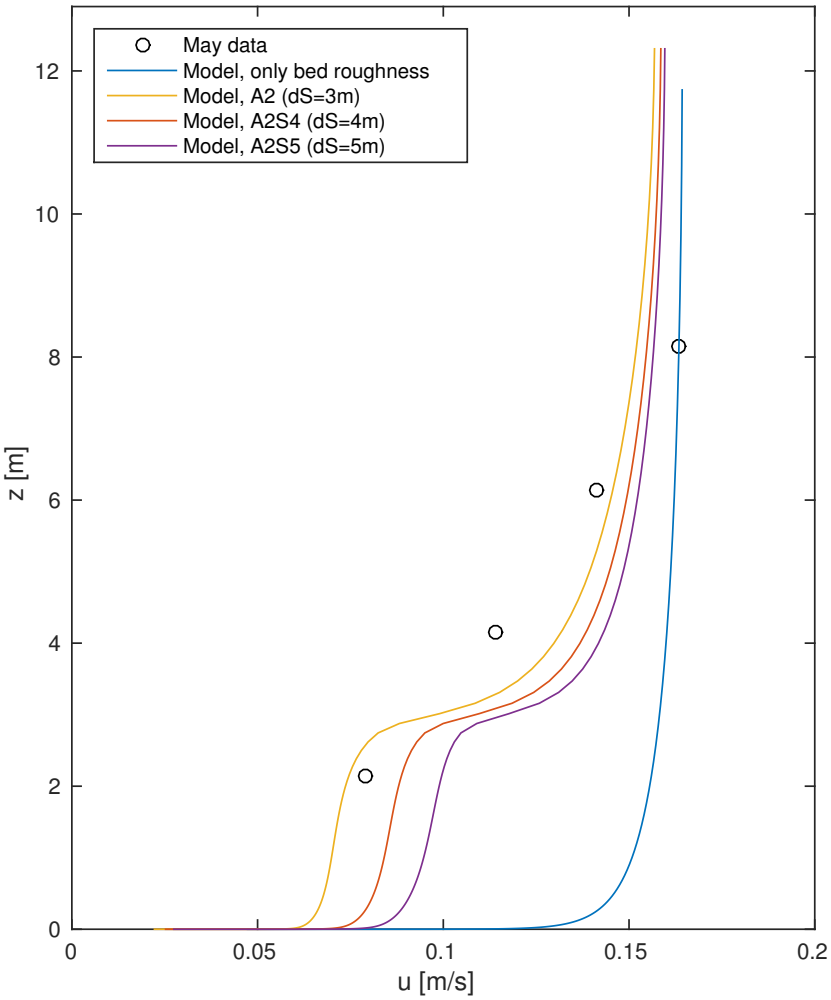

Figure 11.4: Comparison between the modelled velocity profile using different stem spacings ΔS, the field data from May, and the modelled velocity using only the bed roughness ($z_0 = 0.0006\,cm$). u is the spatially averaged mean velocity and z is the water depth.

In figure 11.4, case A2 is recomputed using larger stem spacings ΔS. The results are compared with the May data and with the results using only the bed roughness.

It is seen that the increasing stem spacing results in a larger mean velocity over most of the water column. The increased velocity is most significant within the canopy, and decreases in magnitude towards the free surface.This is in conjunction with the model results in figure 11.3, showing the tendency of the velocity converging towards the free surface.

Changing the stem spacing ΔS is believed to produce larger deviations between the predicted velocity profiles compared to changing the leaf area (in essence the diameter d). This is coupled to the fact that the frontal area per volume a, and hence the canopy

drag force, is a function of ΔS^2 as opposed to being linearly dependent on the diameter d (see equation (5.1.1)). Remembering that the canopy drag force also is part of the wake production (6.2.3) and the wake dissipation (6.3.1) terms, the estimation of the stem spacing becomes of great concern when modelling real life canopies. Even so, all the velocity profiles in figure 11.4 gives improved accuracy with regards to the three lower data points from the Hebrides. There is still a deviation at the highest data point compared with only using the bed roughness.

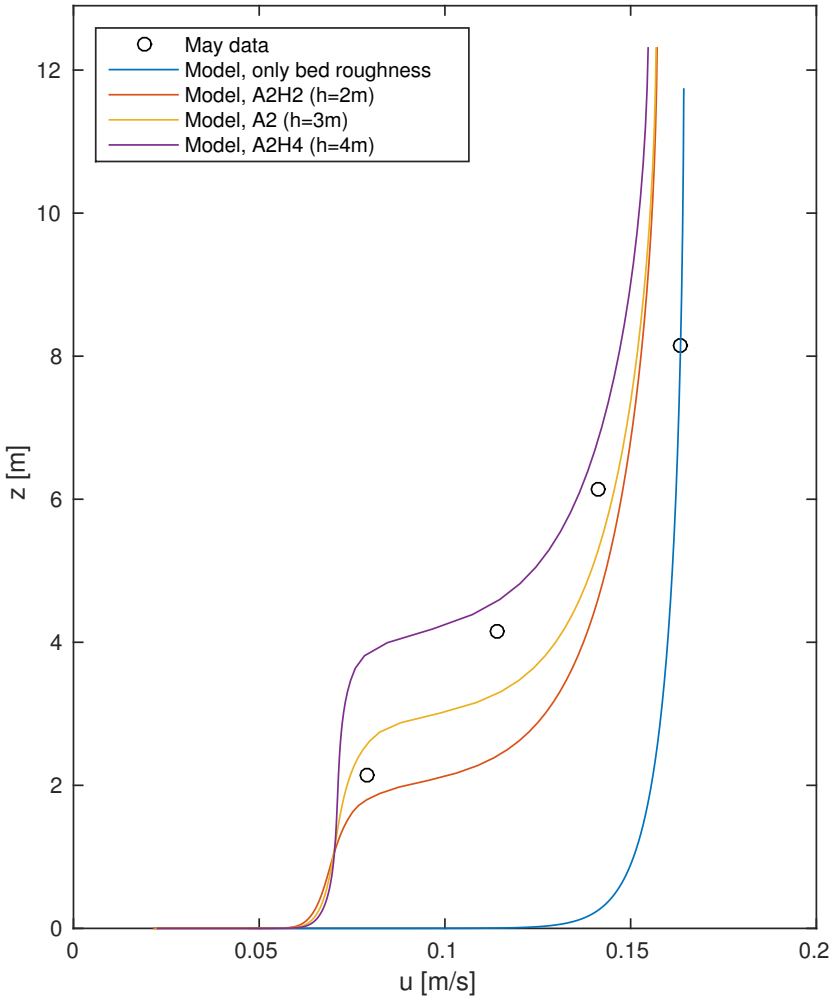

Figure 11.5: Comparison between the modelled velocity profile using different canopy heights h, the field data from May, and the modelled velocity using only the bed roughness ($z_0 = 0.0006\,cm$). u is the spatially averaged mean velocity and z is the water depth.

Figure 11.5 shows the modelled mean velocity profiles using leaf area A2, but with varying canopy height. As expected, the mean velocity within the canopy is unchanged between run A2, A2H2 and A2H4. The only difference is the vertical extend of the canopy drag.

In conjunction with figure 11.3 and 11.4, it seems that the gap in predicted velocity towards the free surface between the present model and the one only using the bed roughness is inherent to the numerical modelling itself, and not so much to the input parameters. It appears that a compromise must be made between accurate velocity prediction toward the surface and accurate velocity prediction towards the sea bed when using the present model.

To summarise, the general observation from figure 11.3–11.5 is that the lower three field measurements for the mean velocity is more accurately predicted by including the effects of the canopy. On the other hand, the velocity measurement closest to the surface is better predicted by only including the bed roughness.

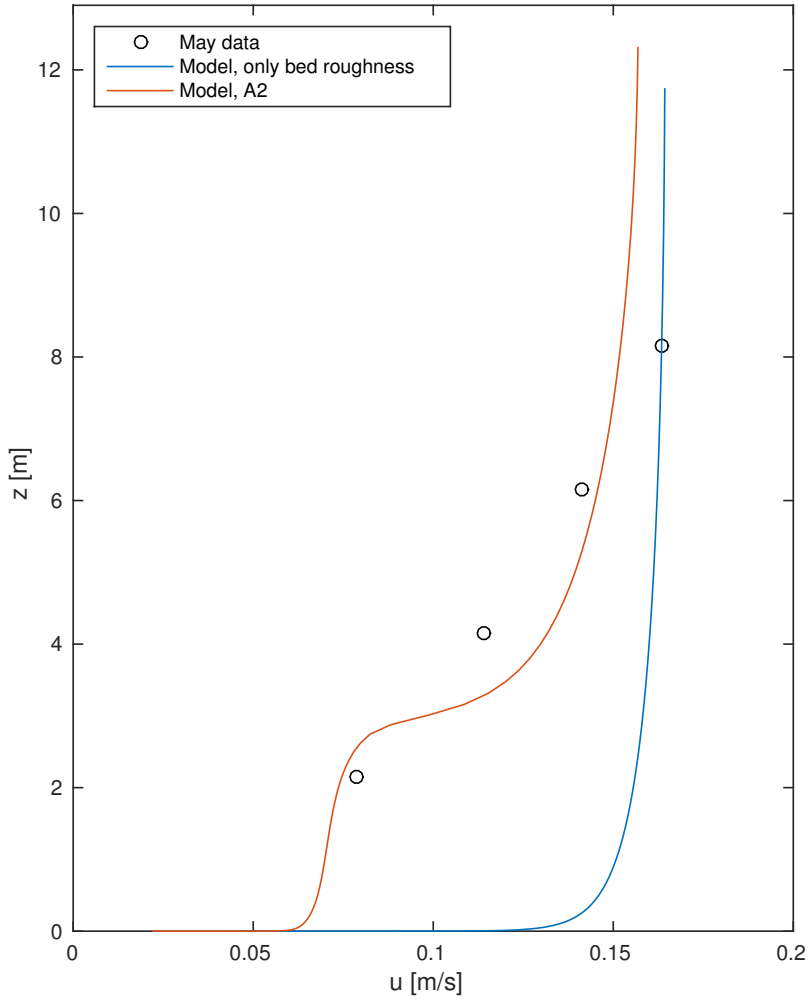

Figure 11.6: Comparison between the most accurate modelled velocity profile from the present model, the field data from May, and the modelled velocity using only the bed roughness ($z_0 = 0.0006\,cm$). u is the spatially averaged mean velocity and z is the water depth.

Although there is a large uncertainty connected with the estimated canopy parameters in table 11.1, they appear to provide reasonable mean velocity profiles. The best fit is probably the one of A2. As a final comparison, A2 has been plotted in figure 11.6 along with the May data and the pure roughness profile.

Important to remember is that the sea bed is more complex than just the presence of the vegetation. In addition, there are rocks and boulders with the possibility of imposing additional effects onto the field data. These effects are naturally not accounted for by the model.

The present results also contradicts the perception given by Nepf (2012a) that for canopy densities of $\lambda_f << 0.1$, the effect of the canopy can be included into the bed roughness. This does not appear to be the case for the modelled tidal flow. The lowest plant density tested for is the one for A2S5 with $\lambda_f = 0.013$, and the modelled velocity profile still predicts the overall field data better than by only using the bed roughness.

It should be noted that the velocity profiles predicted by the the present model indicates a region of shear at the top of the canopy. As described by Nepf (2012a) (see section 5.3) the presence of a shear layer, with an inflection point, at the top of the canopy is the criteria for the generation of canopy-scale vortices. If these vortices are present in the field measurements from the Hebrides, they will not have been accounted for by the model. The modelled shear layer also contradicts the observations by Nepf (2012a), where no shear layer were observed for flow over canopies with $C_D ah < 0.4$.

Another concern with the present model is that it might be erroneous for such low canopy densities as tested for in the present field measurements. As noted from chapter 6, the dispersive fluxes occurring in the momentum equation, and the conservation equation for turbulent kinetic energy, had to be neglected to arrive at the governing equations used by the present model. Poggi et al. (2004) measured the dispersive stress occurring in the momentum equation to be 35 % of the Reynolds stress when doing experiments with sparse rigid cylinders with density $\lambda_f = 0.03$. The modelled canopy density is of the same order, hence making the presence of these fluxes a significant source of uncertainty regarding the modelled velocity profiles.

12 Conclusion

The presence of the vegetation was incorporated into the Navier-Stokes equations through the inclusion of an extra form drag term. In the k-ε equations, the presence of the vegetation result in an additional production term due to the turbulence generated in the wakes behind individual plants. In addition, an extra dissipation term is added to assist the dissipation of this extra wake-scale turbulence. The form drag and wake-production term are generated when spatially averaging the momentum equations and the conservation equation for turbulent kinetic energy over a large enough area. This is done in addition to the regular temporal averaging in order to account for the heterogeneity in the flow due to the complex geometry of the canopy.

When validating the modified model against flume data for unidirectional flow, it was able to predict the velocity profiles within the canopy well. For canopies of relative low density the velocity profile was accurately reproduced throughout the whole water column. For relatively dense canopies the above-canopy flow became overdamped compared to the flume data. However, this tendency appeared to disappear if the water depth to canopy heigh ratio (H/h) was small. A possible explanation to this observation is that the generation of canopy-scale vortices are limited by the free surface for small H/h-ratios. Because the canopy-scale vortices are not accounted for in the numerical model, this might explain the improvement in predicted velocities for the flume experiment with low H/h-ratio. Overall, the flume experiments indicated acceptable accuracy for the implementation of the canopy-related terms into the numerical model.

For the case of wave-current flow, an accurate prediction of the flume data were obtained from superposition of the hydrostatic pressure gradient from the waves and the hydrostatic pressure gradient from the current. When comparing the procedure with the case of a similar flow without waves present, it was found that the wave-current flow needed a significantly larger current induced pressure gradient to obtain a similar depth averaged velocity. However, further validation is needed to assess the applicability of including wave-current interaction when modelling tidal flow over submerged canopies.

When accounting for the submerged vegetation, the model is able to reproduce the field data from the Hebrieds with good accuracy. In particular, the prediction of the mean velocity of the lower half of the water column is significantly improved compared to only using a bed roughness parameter. This may be of significant relevance for applications where the near-bed velocity is of importance.

The upper part of the water column appears to be better predicted when only applying the bed roughness. In comparison the present model overdampes the mean velocity profile in this region. This is a modelling related problem as the canopy-related terms obviously effects the above-canopy flow as well as the in-canopy flow.

Due to the presence of an inflection point in the modelled velocity profiles for field data, there exist a possibility of canopy-scale vortices being generated near the top of the canopy. The generation of these vortices are not accounted for in the model. Also, due to the canopy being very sparse, neglecting the dispersive terms in the derivation of the

canopy related governing equations may not be strictly valid. However, this must be further looked into.

Although the modelled vegetation for the tidal flow is sparse, the results show that the effect of the vegetation can not simply be included in the bed roughness. The inclusion of the vegetation in the momentum and k-ε equations produce an overall better prediction of the tidal boundary layer, especially in the region closest to the sea bed.

13 Further work

The present model have shown great improvement in predicting the overall mean velocity profile of a tidal current. Some areas of investigation still remain.

Although a solution for the canopy-scale vortices already has been proposed, more investigation has to be put into its applicability and limitations before it can be included into the model. Also, the presence itself of canopy-scale vortices for highly sparse canopies has to be further looked into.

More work should also be directed towards the applicability of the model with regards to the dispersive fluxes. These fluxes may be of significant importance for very sparse canopies, and their impact on the predicted velocity profiles should be further investigated.

Last, the attempt to include wave-current effects into the prediction of flow over submerged vegetation should be further validated since only one comparison with experiments were found during this study. It is also unclear how wave-current effects can be included into analysis for tidal flow through submerged vegetation.

Bibliography

Baptist, M., Babovic, V., Rodriguez Uthurburu, J., Keijzer, M., Uittenbogaard, R. E., Mynett, A., and Verwey, A. (2007). On inducing equations for vegetation resistence. *Journal of Hydraulic Research*, 45:435–450.

Cengel, Y. A. and Cimbala, J. M. (2010). *Fluid Mechanics, Fundamentals and Applications*. McGraw-Hill, 2nd edition.

Defina, A. and Bixio, A. C. (2005). Mean flow and turbulence in vegetated open channel flow. *Water Resources Research*, 41(7).

Dijkstra, J. T. and Uittenbogaard, R. E. (2010). Modeling the interaction between flow and highly flexible aquatic vegetation. *Water Resources Research*, 46(12).

Dunn, C., López, F., and García, M. (1996). Mean flow and turbulence structure induces by vegetation: Experiments. Technical Report Hydraulic Engineering Series No. 51, UILU-ENG 96-2009, Dept. of Civ. Engrg., University of Illinois at Urbana-Champaign, Urbana III.

Ghisalberti, M. and Nepf, H. (2006). The structure of the shear layer in flows over rigid and flexible canopies. *Environmental Fluid Mechanics*, 6:277–301.

Ghisalberti, M. and Nepf, H. M. (2002). Mixing layers and coherent structures in vegetated aquatic flows. *Journal of Geophysical Research*, 107(C2, 3011):1–11.

Ghisalberti, M. and Nepf, H. M. (2004). The limited growth of vegetated shear layers. *Water Resour. Res*, 40:1–12.

Grønningsæter, E. K. (2015). Tidal boundary layer flow in coastal zones. thesis, Norwegian University of Science and Technology, Department of Marine Technology.

Hinze, J. (1975). *Turbulence*. McGraw-Hill, Inc., 2nd edition.

Holmedal, L. E. and Myrhaug, D. (2013). Combined tidal and wind driven flows and bedload transport over a flat bottom. *Ocean Modelling*, 68:37–56.

Hu, Z., Suzuki, T., Zitman, T., Uittewaal, W., and Stive, M. (2014). Laboratory study on wave dissipation by vegetation in combined current-wave flow. *Coastal Engineering*, 88:131–142.

King, A. T., Tinoco, R. O., and Cowen, E. A. (2012). A k-ε turbulence model based on the scales of vertical shear and stem wakes valid for emergent and submerged vegetated flows. *Journal of Fluid Mechanics*, 701:1–39.

Launder, B. and Spalding, D. (1974). The numerical computation of turbulen flows. *Computer Methods in Applied Meschanics and Engineering*, 3:269–289.

López, F. and García, M. H. (1998). Open-chnnel flow through simulated vegetation: suspended sediment transport modeling. *Water Resources Research*, 34(9).

López, F. and García, M. H. (2001). Mean flow and turbulence structure of open-channel flow through non-emergent vegetation. *Journal of Hydraulic Engineering*, 127:392–402.

Ma, G., Kirby, J. T., Su, S.-F., Figlus, J., and Shi, F. (2013). Numerical study of turbulence and wave damping induced by vegetation canopies. *Coastal Engineering*, 80:68–78.

Meriam, J. L. and Kraige, L. G. (2013). *Engineering Mechanics - Dynamics*. John Wiley and Sons, Inc, 7th edition.

Myrhaug, D. (2012). *Oceanography: Current, Compendium in TMR4230*. Akademica Forlag.

Neary, V. S. (2003). Numerical solution of fully developed flow with vegetative resistance. *Journal of Engineering Mechanics*, 129:558–563.

Nepf, H. M. (2012a). Flow and transport in regions with aquatic vegetation. *Annual Review of Fluid Mechanics*, 44:123–142.

Nepf, H. M. (2012b). Hydrodynamics of vegetated channels. *Journal of Hyraulic Research*, 50(3):262–279.

Nepf, H. M., Sullivan, J. A., and Zavistoski, R. A. (1997). A model for diffusion within emergent vegetation. *Limnology and Oceanography*, 42(8):1735–1745.

Nepf, H. M. and Vivoni, E. R. (2000). Flow structure in depth-limited, vegetated flow. *Journal of Geophysical Research: Oceans*, 105(C12).

Nielsen, P. (1992). *Costal bottom boundary layers and sediment transport*. World Scientific Publishing Co. Pte. Ltd.

Poggi, D., Katul, G., and Albertson, J. (2004). A note on the contribution of dispersive fluxes to momentum transfer within canopies. *Boundary-Layer Meteorology*, 111(3):615–621.

Raupach, M. R. and Shaw, R. H. (1982). Averaging procedures for flow within vegetation canopies. *Boundary Layer Meteorology*, 22:79–90.

Rodi, W. (1993). *Turbulence Models and Their Application in Hydraulics: A state-of-the-art review*. A.A.Balkema, 3rd edition.

Sakamoto, K. and Akitomo, K. (2008). The tidally induced bottom boundary layer in a rotation frame: similarity of turbulence. *Journal of Fluid Mechanics*, 615:1–25.

Salon, S. and Armenio, V. (2011). A numerical investigation of the turbulent stokes-ekman bottom boundary layer. *Journal of Fluid Mechanics*, 684:316–352.

Shimizu, Y. and Tsujimoto, T. (1994). Numerical analysis of turbulent open-channel flow over a vegetation layer using a k-ε turbulence model. *Journal of Hydroscience and Hydraulic Engineering*, 11:57–67.

Stoesser, T. (2009). Large eddy simulation of turbulent flow throug sumberged vegetation. *Transport in Porous Media*, 78(3):347–365.

Uittenbogaard, R. E. (2003). Modelling turbulence in vegetated aquatic flows, paper presened at riparian forest vegetated channels workshop,cent. of adv. stud. of hydrogeol. risks. Mt. Areas, Trento, Italy.

Wilson, R. N. and Shaw, R. H. (1977). A higher order closure model for canopy flow. *Journal of Appl. Meteorology*, 16:1198–1205.

A Spatially averaged governing equations

Equation (A.0.1)–(A.0.4) shows the spatially averaged governing equation as presented by Raupach and Shaw (1982).

Scheme I

Spatially averaging over a large enough area produce the following conservation equation for momentum,

$$\frac{\partial\langle u_i\rangle}{\partial t} + \langle u_j\rangle\frac{\langle u_i\rangle}{\partial x_j} + \frac{\partial}{\partial x_j}\langle u_i'' u_j''\rangle = -\frac{1}{\rho}\frac{\partial\langle p\rangle}{\partial x_i} - \frac{1}{\rho}\left\langle\frac{\partial p''}{\partial x_i}\right\rangle + \nu\nabla^2\langle u_i\rangle + \nu\langle\nabla^2 u_i''\rangle \tag{A.0.1}$$

Angle brackets indicate spatial mean and double primes denotes a spatially fluctuating value. From the left the different terms are; instantaneous change of velocity, convection, Reynolds stress, pressure gradient, form drag, viscous stress and viscous drag. Term 5 and 7 are additions to the normal RANS equations (4.1.6).

Spatially averaging the conservation equation for turbulent kinetic energy produces equation (A.0.2). The turbulent kinetic energy is $k = \frac{1}{2}\langle u_i'' u_i''\rangle$.

$$\left(\frac{\partial}{\partial t} + \langle u_j\rangle\frac{\partial}{\partial x_j}\right)\frac{\langle u_i'' u_i''\rangle}{2} = -\langle u_i'' u_j''\rangle\frac{\partial\langle u_i\rangle}{\partial x_j} - \frac{\partial}{\partial x_j}\left(\frac{\langle u_i'' u_i'' u_j''\rangle}{2} + \frac{\langle p'' u_j''\rangle}{\rho}\right) + \nu\langle u_i''\nabla^2 u_i''\rangle + \frac{1}{\rho}\langle u_i\rangle\left\langle\frac{\partial p''}{\partial x_i}\right\rangle \tag{A.0.2}$$

From the left the terms are; instantaneous change of k, convection, shear production, inertial and pressure transport, viscous term and wake-production term. The two last terms are additional terms compared to the normal k-equation (4.3.2).

Scheme II

First temporal and then spatial averaging of the Navier-Stokes equations results in the following conservation equation for momentum,

$$\frac{\partial\langle\overline{u}_i\rangle}{\partial t} + \langle\overline{u}_j\rangle\frac{\langle\overline{u}_i\rangle}{\partial x_j} + \frac{\partial}{\partial x_j}\langle\overline{u}_i''\overline{u}_j''\rangle + \frac{\partial}{\partial x_j}\langle\overline{u_i'u_j'}\rangle = \\ -\frac{1}{\rho}\frac{\partial\langle\overline{p}\rangle}{\partial x_i} - \frac{1}{\rho}\left\langle\frac{\partial\overline{p}''}{\partial x_i}\right\rangle + \nu\nabla^2\langle\overline{u}_i\rangle + \nu\langle\nabla^2\overline{u}_i''\rangle \tag{A.0.3}$$

Overbars represent temporal mean values, single primes represent temporal fluctuating values, double primes represent spatially fluctuating values, and angle brackets represent spatially mean values. From the left; instantaneous change, convection, dispersive flux/stress, Reynolds stress, pressure gradient, form drag, viscous stress and viscous drag. For this scheme, three additional terms arise compared to (4.1.6). In addition to the viscous and form drag, a dispersive stress term appears.

The same averaging procedure results in the following conservation equations for the turbulent kinetic energy, where $k = \frac{1}{2}\langle\overline{u_i'u_i'}\rangle$,

$$\left(\frac{\partial}{\partial t} + \langle\overline{u}_j\rangle\frac{\partial}{\partial x_j}\right)\frac{\langle\overline{u_i'u_i'}\rangle}{2} = -\langle\overline{u_i'u_j'}\rangle\frac{\partial\langle\overline{u}_i\rangle}{\partial x_j} \\ -\frac{\partial}{\partial x_j}\left(\frac{\langle\overline{u_i'u_i'u_j'}\rangle}{2} + \frac{\langle\overline{u_i'u_i'}''\overline{u_j}''\rangle}{2} + \frac{\langle\overline{p'u_j'}\rangle}{\rho}\right) + \nu\langle\overline{u_i'\nabla^2u_i'}\rangle + \left\langle\overline{u_i'u_j'}''\frac{\partial\overline{u}_i}{\partial x_j}\right\rangle \tag{A.0.4}$$

From the left the terms are; instantaneous change, convection, shear production, inertial transport, dispersive transport, pressure transport, viscous term and wake-production term. Compared to equation (A.0.2), the wake-production term is expressed differently, and there is an additional dispersive transport term.

B Roughness sensitivity

Figure B.1 shows the model run with different bottom roughness's z_0 against the experimental data from Dunn et al. (1996). It illustrates the small dependency between the boundary condition at the bottom of the flume and the overall prediction of the mean velocity profile.

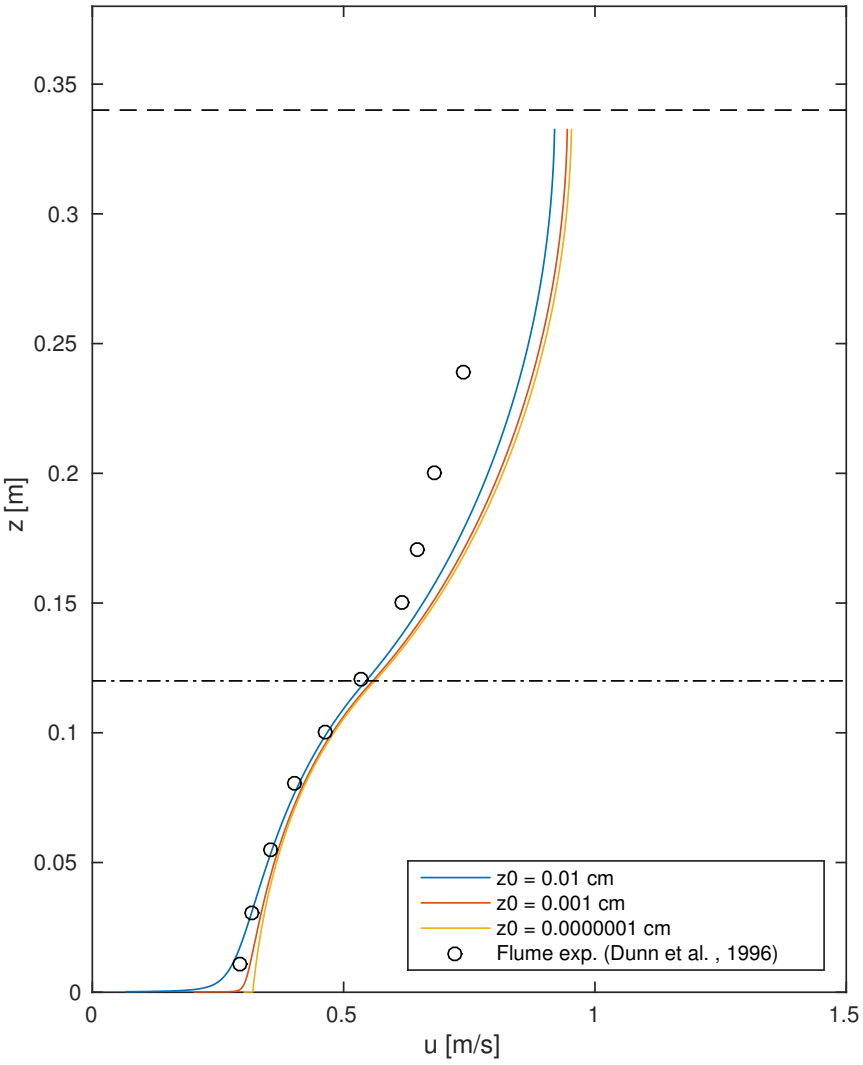

Figure B.1: Modelled velocity profiles for different values of the bottom roughness z_0. Plotted against the experimental data from Dunn et al. (1996). u is the unidirectional spatially averaged mean velocity and z is the water depth. The vertical dashed and dash-dot line indicate the water surface H and the canopy height h, respectively.